Optimizing Methane Uptake on N/O Functionalized Graphene via DFT, Machine Learning, and Uniform Manifold Approximation and Projection (UMAP) Techniques

Rahimi, Mohammad; Mehrpanah, Amir; Mouchani, Parastoo; Rahimi, Ehsan; Salaudeen, Shakirudeen A.

DOI
10.1021/acs.iecr.4c02626

Publication date
2024

Document Version
Final published version

Published in
Industrial and Engineering Chemistry Research

Citation (APA)
Rahimi, M., Mehrpanah, A., Mouchani, P., Rahimi, E., & Salaudeen, S. A. (2024). Optimizing Methane Uptake on N/O Functionalized Graphene via DFT, Machine Learning, and Uniform Manifold Approximation and Projection (UMAP) Techniques. *Industrial and Engineering Chemistry Research*, *63*(44), 18940-18956. https://doi.org/10.1021/acs.iecr.4c02626

I&EC research
Industrial & Engineering Chemistry Research

pubs.acs.org/IECR

Article

Optimizing Methane Uptake on N/O Functionalized Graphene via DFT, Machine Learning, and Uniform Manifold Approximation and Projection (UMAP) Techniques

Mohammad Rahimi, Amir Mehrpanah, Parastoo Mouchani, Ehsan Rahimi, and Shakirudeen A. Salaudeen*

Cite This: *Ind. Eng. Chem. Res.* 2024, 63, 18940−18956

Read Online

ACCESS | Metrics & More | Article Recommendations | Supporting Information

ABSTRACT: Carbon materials possess active sites and functionalities on the surface that can attract prominent interest as solid adsorbents for diverse gas adsorption. This study aimed to predict the optimized methane uptake, adsorption energy (E_{ad}), and adsorbent rediscovery through multitechniques of neural, regression, classifier ML-DFT, and Uniform Manifold Approximation and Projection (UMAP). Nitrogen and oxygen (N/O) functionalities and graphene, graphene oxide (GO), and N-doped GO were applied to the methane storage medium. Multi-ML algorithms were employed for the adsorption energy of CH_4 uptake on (i) N/O functionalities such as pyridinic (N-*py*), carboxyl (O−II), oxidized (N-*x*), hydroxyl (O-*h*), Nitroso (N-*ni*), and Amine (primary, secondary, and tertiary). (ii) The graphene surfaces are decorated with N/O heteroatoms to construct graphene oxide (GO) and N-doped GO. The DFT calculations were applied by PW91 and the Dmol^3 package. N/O-functionalities in the distance of ∼2.0 to 3.1 Å groups obtained E_{ad} of approximately −2.0 to −4 eV. Further, ML models accomplished the forthcoming rediscovery of CH_4 physisorption by using the multiadsorptive features of optimized adsorbents with an R^2 of 0.99. ML-derived sensitivity analysis approach was applied to specifications such as deformation adsorption energy, N/O functionality type, and optimized structure. CH_4 adsorption specifications indicate sensitivity levels of −0.03 to 0.02 eV. The synergetic DFT/ML approaches distinguished the modeled and rediscovered phases of CH_4 adsorption on N/O functional groups and graphene structures. UMAP is employed as a new adsorbent screening approach to play a complementary role in the ML modeling process.

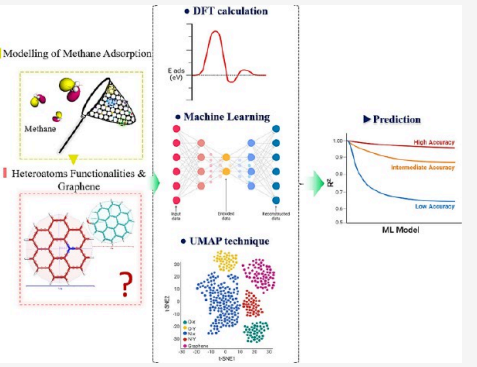

INTRODUCTION

Methane (CH_4) is one of the enchanting green fuels that includes a high portion of natural gas resources (∼90%) with more affordability compared with gasoline and diesel fuels.[1] This principle leads to substantial research that has been prompted by cost-effectiveness amidst increasing global energy demands.[2] The most efficient thing about CH_4 is storage under pressure >200 bar or liquefying at low temperatures within 110 K. Methane can be substantially stored on porous sorbents under low pressures from 35 to 65 bar at room temperature.[3] Thence, the physical adsorption of CH_4 demonstrated facile potential for energy applications, such as sequestering methane from landfill gases,[4] and capturing methane from biogas emissions,[5] which can descend greenhouse gas emissions. Moreover, the prevalent component of biogas, CH_4, becomes a potent greenhouse gas while the organic wastes are untreated in natural conditions;[6] that can be directly stored as a clean energy source for vehicles,[7] and industrial applications.[8] Hence, CH_4 can be regarded as a sustainable energy solution that has attracted interest in planning the synthesis of innovative gas-adsorbent materials. Solid adsorbents are catalysts that can provide solutions for environmental concerns,[9,10] and the rapid depletion of fossil fuels aimed at developing alternative energy storage and conversion systems.[11]

Carbon materials such as bioderived carbon,[12] porous carbon,[5] activated carbon,[13] and graphene[14] are regarded as important components in gas storage.[15] It can be noted that efficient storage through adsorption mechanisms makes it usable on clean and renewable routes.[16] Thence, the in-depth evaluation of physisorption conditions requires understanding control over CH_4 molecules. It can prominently improve the process efficiency in industrial catalysis and petrochemicals in gas storage.[17] The advanced carbon adsorbents have sparked exploration into storage solutions utilizing materials like graphite, graphene, and bundles of nanotubes through a physisorption mechanism.[18] This interaction is often charac-

Received: July 26, 2024
Revised: October 15, 2024
Accepted: October 17, 2024
Published: October 25, 2024

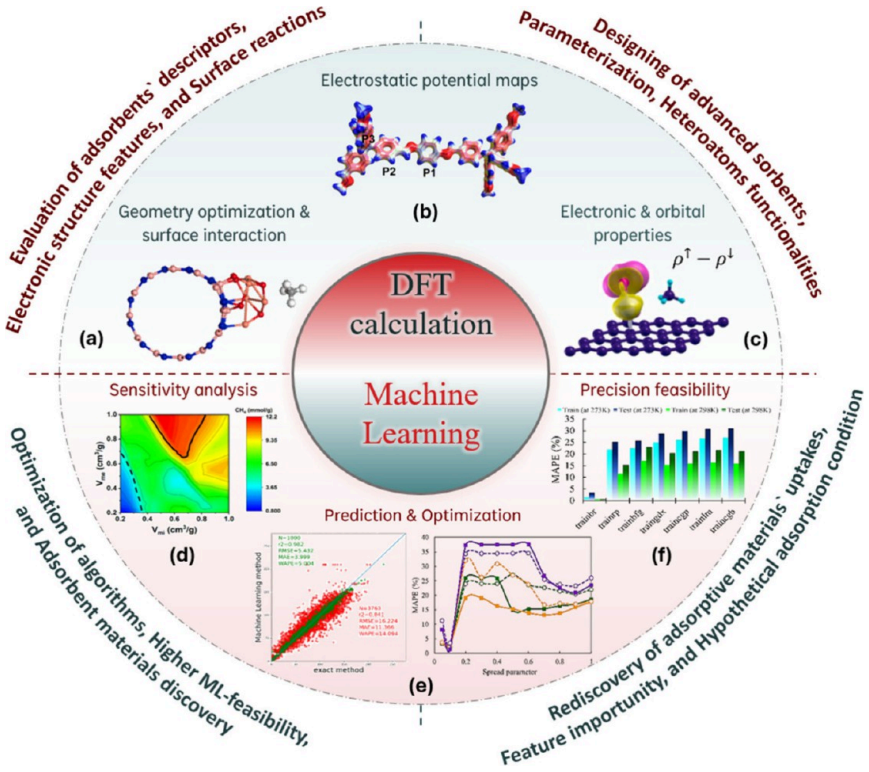

Figure 1. A review of DFT calculation and ML modeling for CH_4 adsorption predictions with approaches of (a) Geometry optimization and surface interaction. Reproduced with permission from ref 51. Copyright 2020 Elsevier. (b) Electrostatic potential maps. Reproduced with permission from ref 52. Copyright 2022 American Chemical Society. (c) Electronic and orbital properties. Reproduced with permission from ref 53. Copyright 2018 Elsevier. (d) Sensitivity analysis. Reproduced with permission from ref 43. Copyright 2021 Elsevier. (e and f) Prediction, optimization, and precision feasibility, respectively. Reproduced with permission from ref 21. Copyright 2022 American Chemical Society.

terized by weak van der Waals forces that, due to the mechanism, allow methane molecules to attach to surfaces without forming chemical bonds.[19] The functionalized carbon materials stand out as excellent candidates for selective adsorption of multigases such as CH_4/CO_2 Nitrogen/oxygen-based (N/O) functionalities (such as pyridinic, graphitic, amine/carboxyl, carbonyl, and hydroxyl) make the carbon surface heterogeneous by the artificial and green-self-doping processes in the carbon matrix of nanostructures.[20] It can usefully raise adsorption enthalpy by boosting the energy-level of the neutral graphene surface.[21] N/O functions can effectively operate as active sites for CH_4 adsorption,[22] which affects the surface interacts with methane molecules, changing its chemical reactivity and attraction toward them. The dynamics of π-electrons can create temporary electron clouds that can stabilize methane on the functionalized carbon surface by creating localized charges.[23]

As a further point of view, the functionalized porous carbon materials have a prominent potential to be employed in gas storage, mainly CH_4, including the amine groups (amine-primary, amine-secondary, amine-tertiary),[6,24,25] nitroso (N-*ni*) and onitroso (N-*on*),[26] nitrogen-pyridinic, and pyrolytic,[27] graphitic,[28−30] and oxidation process.[31] Nitrogen functionalities can contribute to electronic states on carbon matric around the Fermi level.[32] These nitrogen functionalities can enhance extended adsorption sites and the electron density on graphene for methane as nonpolar molecule.[33] Besides, the oxygen functionalities such as carboxyl and hydroxyl can promote the adsorption sites for the internal structure of graphene.[34] In the context of carbon-based materials functionalized with amine groups, a previous study examined the grafting of primary to tertiary amines onto SBA-15 to investigate their influence on CO_2/CH_4 adsorption, exploring factors affecting the process.[35] At a temperature of 25 °C, the results demonstrated that secondary and tertiary amines with an amine density of 1.6−1.7 mmol g^{-1} exhibited a CH_4 uptake equivalent to <0.04 mmol g^{-1}. Conversely, the primary amines adsorbed 0.05 mmol g^{-1}, suggesting more vital interaction forces with CH_4. In another research, 19 graphene nanoflakes (GNFs) were evaluated, each featuring two amines positioned at different locations on the zigzag and armchair corners.[10,24] The results demonstrate a modification in CH_4 uptake when two isolated amines were positioned on two zigzag edges (P4-Z2Z2). Meanwhile, two adjacent amines were placed on a corner and a zigzag edge (P1−C1Z1). As an alternative investigation, the functional groups showed that CH_4 adsorption decreased, attributed to the decline in C═C, −OH, C═O, and $-CH_2$ contents in porous carbon; in which the gas adsorption potential follows the order: C═C > −OH > C═O > $-CH_2$.[36] Although microporous carbon materials can affect the nonchemical reactions of the physisorption mechanism, the functionalities can promote the active sites for CH_4 uptake. Mahmoudian et al. indicated that methane adsorption capacity had no notable impact despite having ultrahigh specific surface area values exceeding (3000 m^2 g^{-1}). Thence, the appraisement of chemical specifications in the carbon solid adsorbents and graphene is a crucial nonstructural assessment within CH_4 physisorption.[28]

Density functional theory (DFT) can determine an incommutable position in the research of molecule adsorption behavior and different adsorption energies (E_{ad}) of adsorbents′ sites. The gas adsorption behavior is significantly affected by the

https://doi.org/10.1021/acs.iecr.4c02626
Ind. Eng. Chem. Res. 2024, 63, 18940−18956

energy levels of their electronic structure, which are determined by the Highest Occupied Molecular Orbital (HOMO) and Lowest Unoccupied Molecular Orbital (LUMO).[37] The frontier molecular orbitals in graphene-based materials play a crucial role in determining the degree of interaction between gas molecules and the outermost layer of the adsorbent.[38] The adsorption features of CH_4 physisorption to fulfill application requirements mandate a thorough understanding of the interplay between the HOMO−LUMO energies and the energy gap. Besides, the molecular interactions of CH_4 molecules with heteroatoms (e.g., nitrogen and oxygen) can be helpful for graphene or N/O doped graphene surfaces.[39] In other words, the physisorption of methane onto graphene surfaces is a multifaceted phenomenon governed by intricate interactions between the methane molecules and the graphene lattice,[40] as well as the presence of various functionalities sites that modify the surface properties.[41] As another alternative approach, when delving into the impact of defects on graphitic substrates, Dutta et al.[30] employed van der Waals-corrected DFT to explore the potential for engineering the morphology of sp^2 carbon substrates to enhance gas uptake and separation, focusing specifically on CO_2/CH_4 binding.[42]

Their findings illustrated a significant disparity in the adsorption of CO_2 and CH_4, particularly on folded graphene sheets and concave curvatures, suggesting the potential utility of this phenomenon for CH_4/CO_2 flow separation. The electric field (EF) is an important factor for methane storage materials' adsorption/desorption performance. Han et al. evaluated oxygen-rich graphene, such as hydroxylated-/carboxylated graphenes (GO−OH and GO−COOH, respectively), via DFT calculation. The adsorptive properties of oxygen groups such as −COOH and −OH improved CH_4 uptake.[45] Moreover, methane oxidation involves the incorporation of metal dopants. A previous study highlighted the effectiveness of platinum doping onto carbon nanoparticles, specifically with Pt loading (at 10 wt %) as a catalyst for the selective aerobic oxidation of methane to produce formaldehyde.[46] These Pt-supported carbon nanoparticles offer a notable advantage due to their high platinum dispersion combined with low reactivity toward the reaction product, formaldehyde. In another study, exceptional active and durable platinum−nickel hydroxide-graphene ($Pt/Ni(OH)_2$/rGO) ternary hybrids were successfully prepared.[47] These hybrids feature small-sized Pt nanocrystals intimately integrated with highly defective $Ni(OH)_2$ nanostructures, all supported on conductive *r*GO nanosheets. The physiosorbed methane molecule on the graphene sheet has enhanced adsorption energy with a high number of carbon atoms, and the values are −0.184 and −0.185 eV (pristine graphene) and −0.188 and −0.191 eV (defective graphene).[48] According to Kandagal et al.,[49] selective functionalization for specific graphene surface spots significantly increases the localized adsorption index. This suggests a potential approach to customizing materials with increased methane storage capacity. Seema et al.[50] found that at 1 bar and 0 °C, sulfur-doped reduced graphene oxide had a low methane adsorption capacity of just 0.75 mmol g^{-1}. The synthesized material showed an adsorption capacity at low partial pressures of $P/P_0 = 0.2$, with an adsorption value of 1.82 mmol g^{-1}.

In the new decade, machine learning (ML) is the most applicable artificial intelligence (AI) tool for multidisciplinary gaseous studies, such as CH_4,[54] CO_2,[55,56] and CH_4/CO_2[44] adsorption properties. The most recent ML and DFT approaches in the gas adsorption fields are illustrated in Figure 1. In a stream of alternative research, Meng et al. used an artificial neural network (ANN) model to predict the CH_4 adsorption behavior of CO_2/CH_4 on anthracite and bituminous coals at different temperatures (35, 45, and 55 °C). Also, the conditional features, such as pressure and solid carbon-based sorbent, are ranked in absolute and actual adsorption amounts. The ANN model obtained predictive accuracies from ∼0.98 to 0.99 of R^2. The lone pair electrons in heteroatom functionalities, specifically nitrogen and oxygen electrons, strongly attract attention to gas capture. Rahimi et al. applied the radial basis function-neural network (RBF-NN) on N/O dual-doped porous carbon materials for CO_2 uptake predictions. The RBF-NN estimated the performance of CO_2 uptake based on the microstructural and nitrogen groups under pressures ranging from 0.15, 0.6, and 1 bar at 298 and 273 K (room and cryogenic temperatures). The ML algorithm achieved the lowest mean absolute percent error <3.5% by determining the CO_2 capture with 0.97 to 0.99 of R^2.[21] The literature review of ML and DFT data-driven techniques' applications within gas adsorption is provided in Table 1. Further, the presence of N-nitroso and -onitroso groups introduces polar components that improve the adsorptive feature of carbon materials by facilitating dipole−induced dipole interactions.[57] Oxygen functionalities, such as epoxy and ether groups, affect the surface polarity. It modifies the electronic structure of graphene carboxyl groups, which have the ability to establish hydrogen bonds with methane molecules, resulting in increased adsorption stability.[58] Uniform Manifold Approximation and Projection (UMAP) is a novel dimension reduction technique that attracted significant attention for its ability to preserve the structure of data sets and material screening. Daun et al. applied UMAP to visualize 10% of a random sample of thousands of hypothetical complexes.[59] Also, UMAP can be used to create a low-dimensional data source that is suitable for clustering. Baird et al. utilized the algorithm of DensMAP to directly achieve density estimations within the dimensionality reduction step.[60]

This study aimed to use multiple ML algorithms, DFT, and UMAP techniques for CH_4 adsorption to construct DFT-based ML workflows. DFT evaluates the comprehensive N/O functionalities with ML models to predict the adsorption energies for CH_4 uptake. In the meantime, much experimental research has been conducted on the effects of various heteroatoms on the physisorption of methane, including nitrogen.[61] Also, according to the above-mentioned literature, the ML technique is applied chiefly based on microstructural and conditional features. Although recent data-driven ML works could predict gas uptake, ML has not yet been used for the following:

i. Single heteroatom functionalities combined with graphene and GO as solid CH_4 adsorbents.
ii. DFT-based ML optimizes the adsorption energies based on the 14 N/O functionalities and three graphene structures.
iii. Sensitivity levels of adsorptive/chemical features such as functional group types and deformation energy CH_4 uptake.
iv. Three classes of neural, regression, and classifier ML algorithms applied for CH_4 adsorption.
v. UMAP visualized the adsorbent types by screening the data sets of adsorbents.

The contributions lie in evaluating the in-operando performance of N/O functionalities on graphene, which can significantly

https://doi.org/10.1021/acs.iecr.4c02626
Ind. Eng. Chem. Res. 2024, 63, 18940−18956

Table 1. Recent Literature on ML Applications Using the Data-Driven Technique in Gas Adsorption[a]

Approach	Process and Achievements	Ref
ML models were constructed based on 1774 data points containing microstructural (micro/mesopore volume, surface area, etc.) and operational features (temperature and pressure) to evaluate the CO_2/CH_4 selectivity uptake on porous carbon.	RF exhibited a higher importance level on microstructural surfaces than pore volumes with an estimation accuracy of 0.99 R^2.	43
CO_2/CH_4 adsorbed on three types of coal was analyzed using the ANN model's temperature, pressure, and coal rank descriptors.	ANN model with 15 neurons/*tanh* function used features such as pressure, porosity, liptinite, vitrinite, and *R*-max ranked 0.72, 0.09, and 0.05 to ~0.065 scores with 0.97−0.99 of R^2.	44
ML-DFT model predicted CO_2 uptake on N/O rich functional porous carbon by the GA algorithm with RBF and DFT calculation techniques at 273 and 293 K under 0.15 to 1 bar.	RBF-DFT optimized E_{ad} of HOMO−LUMO. E_{ad} is achieved in a range of −15.9 to −17.4 kJ mol^{-1}. N-X and N-Q showed importance on gas uptake with accuracies ~3.5% of MAPE and R^2 range of 0.97−0.99.	21
DFT calculation was employed on methane storage performance on GO, which was decorated with oxygen functionalities such as GO-OH/-COOH/-COC.	GGA and PBE functional utilized to describe electron exchange-correlation	45
DFT+ML calculated N/O functionalities groups and graphene-derived adsorbents to estimate CH_4 adsorption energy (E_{ad}). Five ML models were applied to evaluate the feasibility of ML modeling for methene E_{ad} rediscovery.	Five ML models performed highly accurate predictions with R^2 of 0.93 to 0.99.	*This work*

[a]ANN = Artificial neural network; GGA = Generalized gradient approximation; PBE = Perdew−Burke−Ernzerhof (PBE); GO−OH/-COOH/-COC = hydroxylated, carboxylated, and epoxy-modified graphene oxide; GA = Genetic algorithm.

influence methane adsorption. Hence, solid adsorbent structures were established to assess the performance of CH_4 physisorption. The contributions of methane storage on solid adsorbents can be pointed out below:

- Calculate the adsorption energies of CH_4 molecules on various graphene structures such as graphene, graphene oxide (GO), N-doped GO, and heteroatom functionalities.
- Assessments of CH_4 uptake's feasibility on comprehensive N/O functional groups (such as hydroxyl, carbonyl, carboxyl, epoxy, ether; and pyridinic, pyrolytic, graphitic, oxidized, amine primary, secondary, and tertiary, nitroso and onitroso, respectively.)
- Synergistical DFT-based ML and UMAP approaches to model and rediscovery of CH_4 adsorption and adsorbents.

Hence, DFT-based ML was applied to 150 data sets by using algorithms such as support vector regressor (SVR), Decision Tree Regressor (DT), Multilayer Perceptron (MLP), and k-nearest neighbors (KNN) for an in-depth study of CH_4 uptake. DFT-ML can usefully disclose the adsorptive behavior of heteroatom-functionalized graphene structure interactions with methane at the molecular level. Moreover, ML techniques include the independent variables such as the optimized geometries of adsorbents and N/O functional group types (OS and FT, respectively) for predicting the energy absorption of methane as provided in the Material and Methods section. Further, UMAP analysis disclosed a high potential for discovering complex materials. Although DFT-ML can enhance the fundamental understanding of gas adsorption phenomena, it also facilitates the systematic modification of graphene-based adsorbents for higher gas storage and separation applications.

MATERIALS AND METHODS

2.1. Structures and Principle Calculations. This study applied DFT calculations to CH_4 adsorption on multiple adsorbents and continued with ML techniques to rediscover CH_4 energy adsorption, as illustrated in Figure 2. Structures of graphene sheets and N/O heteroatom functionalities are designed to depict the configuration of solid adsorbents, where each sheet has a length of 20 Å along the *x* and *y* directions. Each single-graphene sheet and heteroatom functionalities were performed to evaluate how active sites on graphene oxide or N/O-dual doped graphene can affect the CH_4 adsorption. Specifically, the combined molecular dynamics simulation assisted with machine learning techniques is established to evaluate the feasibility of multifunctional groups and graphenes for methane adsorption. Therefore, 14 nitrogen and oxygen functionalities and three graphene structures are assumed to include sites in the carbon matrix, as presented in Table 2. The nitrogen functional groups are (i). pyridinic (N-*py*), (ii). pyrrolytic (N-*pyr*), (iii). graphitic (N-*q*), (iv). oxidized (N-*x*), v, vi, and vii). amine primary, -secondary, and -tertiary (N-*p*, N-*s*, and N-*t*), viii, and ix). nitroso (N-*ni*), and onitroso (N-*on*). On the other hand, oxygen functional groups consist of five functionalities: hydroxyl (O-*h*), carbonyl (O−II), carboxyl (O−III), epoxy (O-*x*), and ether (O-*eth*).

2.2. DFT Calculation. A DFT calculation procedure was employed to provide molecular-based insights into the adsorption mechanism before the optimization process of the ML technique. These calculations were proceeded by using the Gaussian code in Materials Studio package 2017.[62] PW91 is considered as generalized gradient approximation (GGA)

https://doi.org/10.1021/acs.iecr.4c02626
Ind. Eng. Chem. Res. 2024, 63, 18940−18956

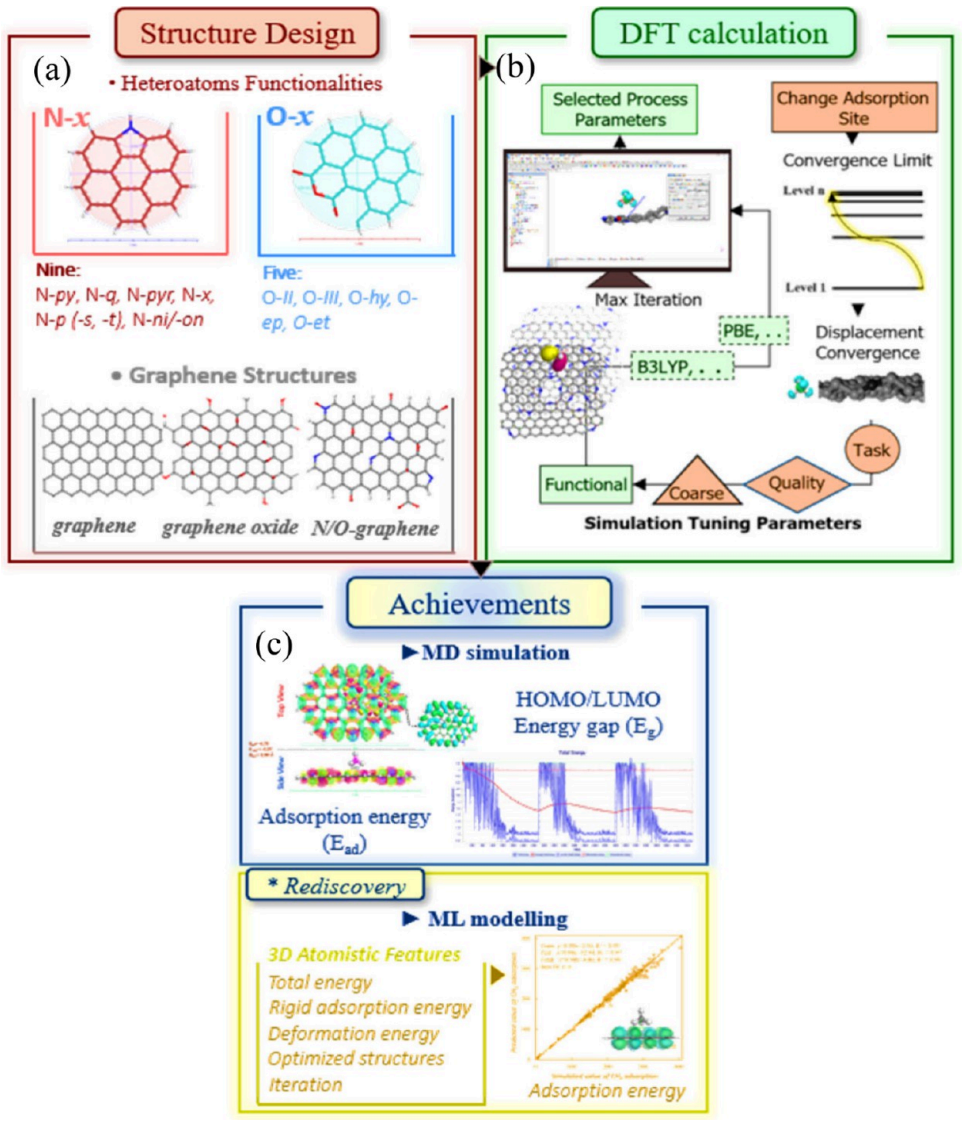

Figure 2. Schematic illustration of the modeling of multiprocesses of CH_4 adsorption on solid adsorbents with (a) structure design of nine/five/three nitrogen-, oxygen functional groups, and graphene sheets (simple, oxide, and N/O-dual doped), (b) DFT calculations, and (c) achievements of DFT by combining with five ML techniques for rediscovery of CH_4 adsorption energies.

Table 2. Optimized Hyperparameters of ML Models

Nitrogen functionalities site	Symbol	Oxygen functionalities site	Symbol
Pyridinic*	N-*py*	Hydroxyl	O-*h*
Pyrolytic	N-*pyr*	Carbonyl	O−II
Graphitic	N-*q*	Carboxyl	O−III
Oxidized	N-*x*	Epoxy	O-*x*
Amine primary, secondary, tertiary	N-*p*, N-*s*, and N-*t*	Ether	O-*eth*
Nitroso	N-*ni*	Graphene oxide	GO
Onitroso	N-*on*	N/O-dual doped graphene	N-GO

functional with the low computational cost to describe the electronic structure of heteroatoms functionalities, graphene, graphene oxide (GO), N-doped GO. On the other hand, as this approach merged with ML techniques, the low-cost functional in DFT calculations which adopted to rediscover the methane adsorption on graphene.

The geometry optimizations of CH_4, N/O functional groups, and graphene with the adsorption energy (E_{ads}) calculations related to the best stable geometries were accomplished based on the B3LYP functional. The real-space cutoff was 5.0 Å. The E_{ads} of CH_4 molecule on N-doped graphene oxide (N-GO) as adsorbent was calculated using the following eq 1:

$$E_{ads} = E_{sorbent+CH4} - (E_{sorbent} + E_{CH4}) \quad (1)$$

Where $E_{sorbent+CH4}$ shows the total energy of the carbon-based sorbent/CH_4 adsorbate configuration. $E_{sorbent}$ and E_{CH4} represent the energy of adsorbents such as GO and N-GO with adsorbate (CH_4 molecule), respectively. It can be noted that the E_{ads} value was negatively achieved, which addressed the exothermic adsorption process. Meanwhile, the higher amounts of E_{ads} indicate a desirable interaction between the sorbent and CH_4 adsorbate.

The details of the DFT calculation tuning parameters are presented in Table 3. Moreover, DFT primary calculations, as provided in Figure 2, GGA (generalized gradient approximation) combined with the PAW technique by implementing in

https://doi.org/10.1021/acs.iecr.4c02626
Ind. Eng. Chem. Res. 2024, 63, 18940−18956

Table 3. Tuning Parameters of the DFT Calculation for Methane Adsorption

Parameters of DFT for CH_4	Value
Convergence limit	5.0 e^{-4}
Maximum iteration	50
Energy	2×10^{-5} Ha
Force	0.5 kcal mol^{-1}
Displacement convergence	5×10^{-3} Å

Materials Studio.[63] Moreover, the Perdew Burke Ernzerhof (PBE) function and Hellmann−Feynman force convergence criterion can define the exchange-correlation energy based on the energy convergence criterion to 1×10^{5} eV and 5×10^{2} $eVÅ^{-1}$, respectively. The deformation charge density (ρ_{de}) can be calculated by Equation 2 as below:[64]

$$\rho_d = \rho_{\text{adsorbed state}} - \rho_{\text{graphene}} - \rho_{\text{gas molecules}} \quad (2)$$

where the $\rho_{\text{adsorbed state}}$ presents the charge density of the configuration of graphene-absorbed gas, and the ρ_{graphene} and $\rho_{\text{gas molecules}}$ are the charge density of isolated graphene and gas molecules, respectively. The optimized E_{ad} and HOMO−LUMO energy gaps were evaluated along with multi-ML techniques merged with five adsorption parameters of CH_4, which were the total energy (TE), rigid adsorption energy (RAE), deformation energy (DE), optimized structure (OS) and functionalities type (FT), to predict the adsorption energy of CH_4. The adsorptive independent variables, such as TE, RAE, and DE are DFT-based features after 15 simulation runs. FT and OS are classification variables (as non-numeric input) that indicate the N/O functionalities and optimized graphene structures used to predict the CH_4 uptake. In the next section, the details of the ML process for CH_4 adsorption are discussed.

2.3. Machine Learning (ML) workflows. Machine learning (ML) models comprehensively can be divided into four categories: supervised, unsupervised-, semisupervised-, and reinforcement learning, as illustrated in Figure 3. The comparative abilities of each class are provided in Table 4,[65] which each class includes a particular procedure and specified area for modeling. Supervised learning utilizes a labeled data set known as the training set (x, y). According to the existing training set, the optimal model was obtained via training and continued by applying the obtained mapping to unknown independent variables to achieve the dependent ones. Supervised learning consists of various ML algorithms such as neural (MLP), regression (SVR, DT, and RF), and classifier-based (KNNs) algorithms. A set of supervised ML models was applied to predict the E_{ads} of methane on graphene and heteroatoms functionalities. This study applies ML approaches such as SVR, RF, DT, MLP, and KNN, and the optimized hyperparameters of these ML models are provided (section 2.4). All are merged with DFT calculation processes by considering the methane adsorption energy as *y* or the predictive target. Notably, the prepared data sets were systematically partitioned into 50 to 80% ratio range to facilitate the training and testing phases of the ML procedure. Before the ML model application, the min-max normalizations were implemented as a preprocessing step of the data sets. Furthermore, a cross-validation with 5-fold on the training set was applied for model selection and hyperparameter optimization.[17] Afterward, the optimal model

Table 4. Comparative ML Classes' Predictive Performance

Class	Performance
Supervised learning	• Labeled data set using in training set (*x*, *y*). • Optimal model is selected based on the training phase. • Applying the trained mapping procedure on unknown data sets.
Unsupervised learning	• Data is unknown, and data sets are not labeled. • Training step consist of input and output *x* and *y* that are known/unknown. • Data sets of samples need to be sorted based on similarity.
Semisupervised learning	• Structured by combining supervised- and unsupervised learning. • Raw data points consist of labeled/nonlabeled data to create the pattern.
Reinforcement learning	• Learning process based on trial and error. • Permits learning to do the map situations based on the environment. • Operates by rewarding/punishing sign interaction with the environment.

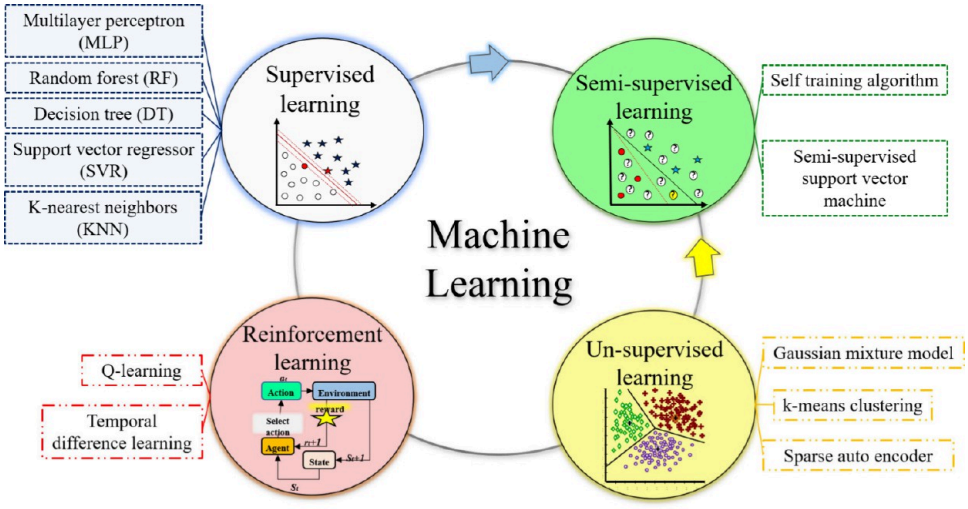

Fig 3. The classification of machine learning models.

Figure 3. Classification of machine learning models.

https://doi.org/10.1021/acs.iecr.4c02626
Ind. Eng. Chem. Res. 2024, 63, 18940−18956

was retrained on the entire training set, and the resultant evaluation metrics were obtained for both the train and test sets. The ideal training/test phases' size selection was applied based on the portions 70/30% of the total ∼150 data sets of CH_4 adsorption in all (17 types of adsorbents such as N/O functionalities and graphene-based structures). Although ML techniques are feasible with a quantitative input set, qualitative inputs can bring novelty for the ML modeling process. The two input features of FT and OS are nonquantitative variables (as classification ones) applied in the ML modeling process to predict the CH_4 adsorption energy.

2.4. ML Algorithms. ML algorithms work based on their respective hyperparameters that need to be optimized to achieve ideal targets, while the challenge is that the default settings of hyperparameters are inadequate to ensure the ideal performance of ML methods.[66] Thus, determining the optimal hyperparameters is critical for ML schemes, as illustrated in Table 5.

Table 5. Optimized Hyperparameters of Five ML Models[68]

Model name	Hyperparameters
Support Vector Regressor (SVR)	C = 100, Gamma = 0.1
Random Forest (RF)[a]	Max depth (MD) = 21; Min samples leaf (MSL) = 1; Max features (MF) = 0.26
	Number of estimators (NE) = 175
Multilayer Perceptron (MLP)	Hidden layers = (100, 100, 100); Activation = tanh; Early stopping = True
Decision Tree (DT)	Max depth = 20
K-Nearest Neighbors (KNNs)	Weights = distance

[a]NE = 10−1000, MF = 0−20, MSL= 1, MD = 5−500.

Principally, two techniques of hyperparameter tuning can be utilized in this study, which are explained below:

i. Trial-and-error: It is a straightforward procedure to tune the hyperparameters of ML algorithms. Using this approach, different hyperparameters can be manually tested, and those presenting the ideal result, or the most negligible error can be chosen for the ML algorithm. For example, four vital tuning parameters in the RF model's structure, namely, *Max depth*, *Min samples leaf*, *Max features*, and *Number of estimators*, were optimized using the trial-and-error approach.[56,67]

ii. Random search (RS): This technique can tune the hyperparameter so that the defined hyperparameters are merged in any criteria or by any order. The tuning process of four ML methods of SVR, MLP, DT, and KNNs was conducted using the RS technique.[69] In the next section, all ML algorithms specifications are discussed and comparatively evaluated based on their computational neural, regression, and classifier classes.

2.4.1. Neural-Based MLP. A Multilayer Perceptron (MLP), also referred to as MLP-neural networks (MLP-NNs), is structured as a feed-forward neural network with one input layer, one output layer, and multiple hidden layers.[70] The number of neurons in the input and output layers is determined by the data set's input and output vectors, while the hidden layers are established through random search. MLP can model the classification and regression for complex nonlinear relationships. Although it can generalize well to unseen data, it is difficult to interpret how they reach their decisions.[71] Each layer consists of neurons connected to neurons in the adjacent layer with specific weights, which are often initialized randomly.[72,73] Table 6 presents the comparative specifications of multineural, regression, and classifier-based ML algorithms. All of the ML algorithms, specifically MLP, are employed to predict the specific feature of CH_4 adsorption (E_{ads}), in which the input

Table 6. Comparative Equations and Performances of ML Algorithms

ML algorithm	Equation	Performance
MLP	$f(\theta) = \frac{1}{1+e^{-\theta}}$	• Neurons' sizes in both input/output layers are specified based on the input and output vectors in data sets.
	$W(n+1) = W(n) - \eta\frac{\partial E}{\partial W} + a(W(n) - W(n-1))$	
	$U(n+1) = U(n) - \eta\frac{\partial E}{\partial U} + a(U(n) - U(n-1))$	• Hidden/output layers create predictions depending on the weighted input's neuron.
	n = the training iterations' value; a = the momentum factor; E & η = the error and the learning rate	
SVR	$f(x) = \sum_{i=1}^{n}(\alpha_i - \alpha_i^*)K(x_i, x) + b$	• Error-insensitive zone size (ε) and the regularization parameter are pivotal elements.
	$K(x_i x) = (1 + x_i' x)^p$, p = 2, 3	
	$K(x_i, x) = exp(-\gamma\|x_i - x\|^2)$	• Gaussian kernel function is accomplished so that a trial-and-error approach can determine the parameters.
	$K(x_i x)$ = kernel function; α_i, α_i^* = the Lagrange multipliers	
RF	$H^{oob}(x) = argmax\sum t = 1^T I(h_t(x) = y$	• Training set can show the trained data sets for tree h_t, and H^{oob} indicates the OOB approximation for sample x.
	$\varepsilon^{oob}(x) = \frac{1}{\|D\|}\sum_{(x,y)\in D} I(H^{oob}(x) \neq y)$	• The randomness-level of the RF algorithm can be controlled by the K parameter, which is defined as $k = \log_2 d$.
	$I(X_i) = \frac{1}{B}\sum_t^B \widetilde{OOB}err_t{}^i - OOBerr_t$	• Each x_i variable might be scrambled by shuffle to specify the feature relevance.
	x_i = transferred ith feature; $\widetilde{OOB}err_t{}^i$ = model's error of the shuffled OOB; $OOBerr_t$ = noninfluenced OOB data samples	
DT	$p(c\|x) = 1D\sum i = 1Dpi(c\|x)$	• Capable of conducting out both continuous and discrete data sets.
	$p(c\|x)$ = The probability of class c (when x is known)	• It is highly feasible to select the optimal discriminatory features.
KNN		• Easily applied to data sets with classification purposes.
	Predictive weight $= \sum_{i=1}^{n}(\frac{w_{i,j}}{\sum_{i=1}^{n} w_{i,j}} y_t{}^i)$	• Different test samples can be predicted with an extended range of nearest neighbors.
	n = the number of training samples; $y_t{}^i$ = the true value of the ith training sample	• k nearest neighbors of test data employed to predict its class label with the majority rule.

https://doi.org/10.1021/acs.iecr.4c02626
Ind. Eng. Chem. Res. 2024, 63, 18940−18956

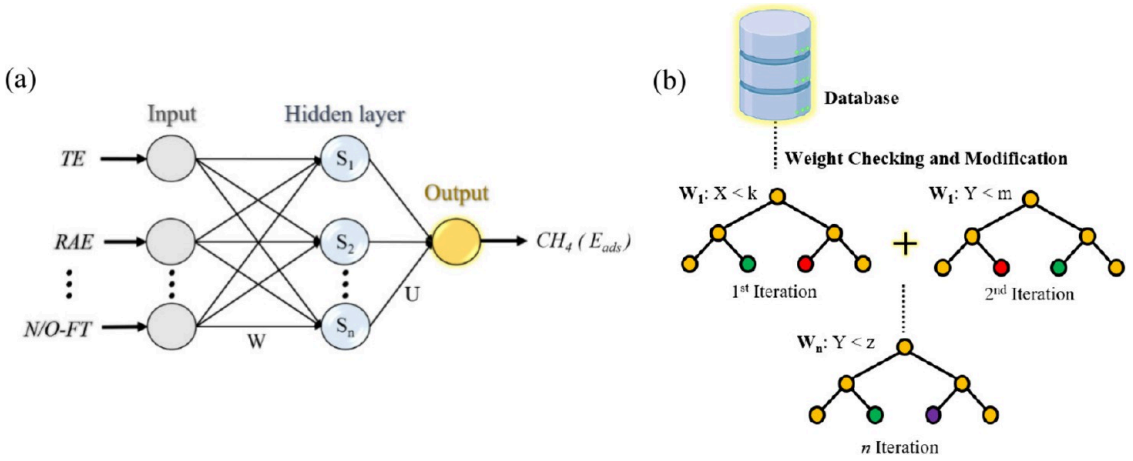

Figure 4. Schemes of (a) the MLP and (b) the RF algorithms are used to predict the CH_4 adsorption mechanism.

layers consist of five inputs: TE, RAE, DE, OS, and N/O-FT. as shown in Figure 4. The hidden layers are composed of neurons denoted as S_1, S_2, S_3, ..., and S_n, while E_{ads} constitute the output layer. This study's configuration includes inputs (the data set for CH_4 adsorption on N/O functional groups and graphene), the hidden layer, and the output (E_{ads}).

2.4.2. Regression-Based SVR, RF, and DT. Random forest (RF) is a classifier/regression ensemble technique that makes predictions by collecting decisions with trees. As the word "forest" shows, many decision trees (DT) are included in the RF model, which is used as the ultimate decision-maker (as illustrated in Figure 4). In the RF algorithm, the random sampling method is regarded as bagging in which one-third of the data sets can be excluded for training in the subtree. RF can build multiple decision trees by preventing overfitting with large data sets and high-dimensional spaces. Noteworthy, it may have high computational cost with many trees with less interpretability.[74]

Decision tree (DT) algorithm is originally rule-based and binary-tree building technique,[73,75] can find the best split that presents the ideal prediction with low error, which is the ML algorithm's goal in supervised learning.[76] Like other neural-network-based ML models, it employs a supervised learning approach grounded in statistical learning theory. DT can introduce clear, interpretable models in fast, and low-cost processes. This algorithm works based on the learned splits; the predictions are unstable with different generated trees.

The primary objective of the SVR model is to identify a function, f(x), for the training data set (x_1, y_1)... (x_i, y_i), to attain the optimal bias (ϵ). SVR can usefully perform with small data sets, with high resistance to the outliers' influence. On the other hand, it requires to be tuned by parameters such as the regularization term (C) and gamma.[77] The comparative performances of regression-based ML algorithms are listed in Table 6.

2.4.3. Classification-Based KNN. In our work, the KNN algorithm is applied to obtain the correlation coefficient matrix W; then, it obtains an ideal value of k for each test sample. Then, we employed the selected k to conduct KNN algorithm for different data sets with various inputs. As an instance-based method, k-NN can predict based on the closest data points in the feature space, which can be determined by a specified number of k of nearest neighbors.[78] Thence, KNN is feasible with small data sets along with fast training processes with a simple decision boundary. It requires feature scaling, such as normalization and standardization.

2.5. Data Preprocessing. According to the different types of data values, two standardization preprocessing techniques data sets: i. Min-max normalization and ii. Conventional normalization was applied before the ML modeling process. Min-max standardization is the most common procedure that can be employed in variables (v) included in data sets as data preprocessing. This method scales the data to a fixed range, typically $[-1, 1]$, that can be defined with Equation 3 as follows:

$$v_n = \frac{v - v_{min}}{v_{max} - v_{min}} \tag{3}$$

where v and v_n indicate the original value of the variable and normalized independent and dependent variable values. v_{min}, and v_{max} represent the maximum and minimum values of the concerned variable, respectively. Conventional normalization, well-known as *Z-score* normalization, can be applied to data for standardization in the range of $[0, 1]$. The process of normalization can be conducted by the linear data sets mapping over a rigid range in which the value of v is stated as Equation 4:[74]

$$v_n = \frac{v - v_{min}}{v_{max} - v_{min}} \times (r_{max} - r_{min}) + r_{min} \tag{4}$$

r_{min} and r_{max} stand for the desired values of the transformed variable range.

2.6. Primary Statistical Analysis. As a primary analytical procedure, the adsorptive DFT features were evaluated through the Pearson correlation coefficient (PCC). In other words, the correlation coefficient index measured the linear dependence between the input variables and the adsorption energy of CH_4. PCC evaluated the collinearity value of two variables and the related linear correlations, which can be determined by Equation 5:

$$\rho_{xy} = \frac{\sum_{i=1}^{n}(v_i - \overline{v})\sum_{i=1}^{n}(t_i - \overline{t})}{\sqrt{\sum_{i=1}^{n}(v_i - \overline{v})^2}\sqrt{\sum_{i=1}^{n}(t_i - \overline{t})^2}} \tag{5}$$

where v and t represent the adsorption input variable and target (or adsorption energy of CH_4); meanwhile $\overline{v}$, and $\overline{t}$ indicate the mean values. Thus, eq 5 varies between -1 and 1 for the linear conversion of two variables. Hence: $\rho_{xy} = -1$, 0, and 1 demonstrate that v and t have entirely negative, obscure, and

https://doi.org/10.1021/acs.iecr.4c02626
Ind. Eng. Chem. Res. 2024, 63, 18940−18956

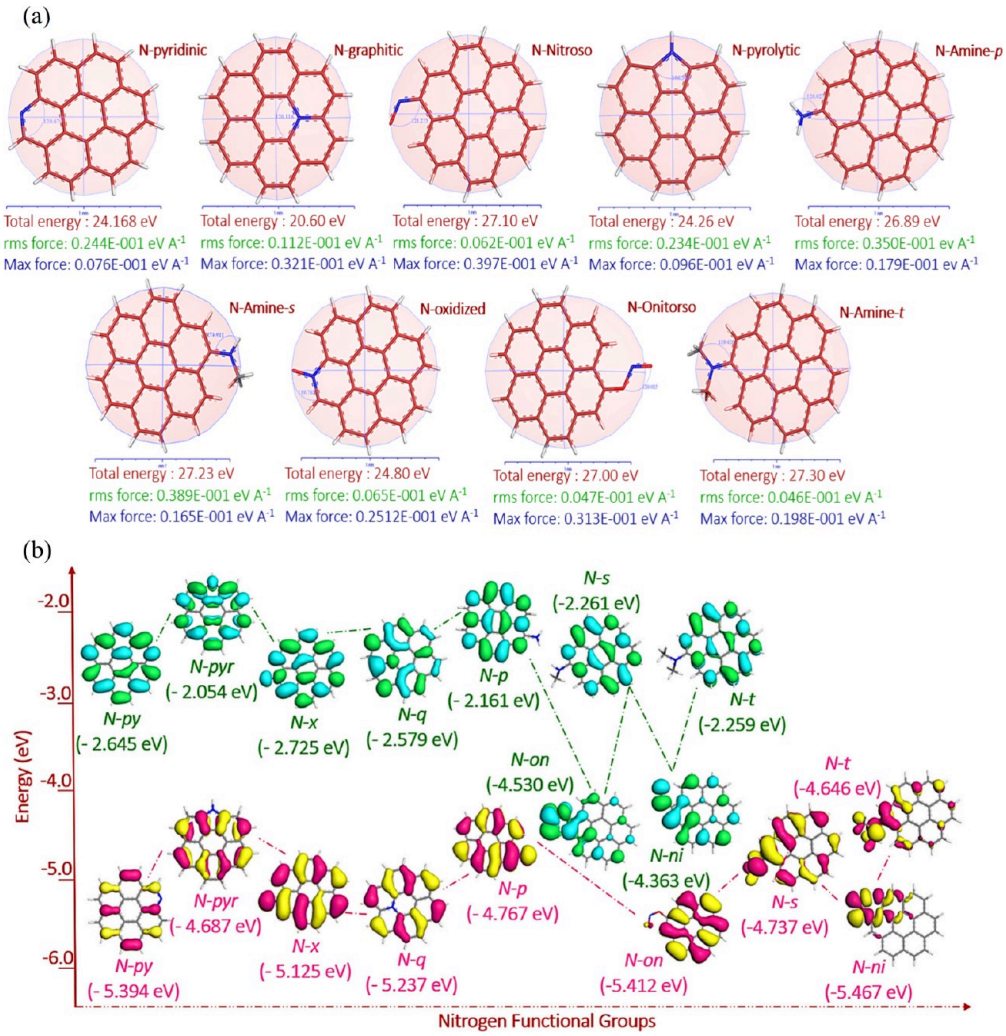

Figure 5. Illustration of (a) the energy-optimized structures of nine nitrogen functionalities as adsorbents of CH_4 and (b) the calculation of HOMO/LUMO energies of CH_4 adsorption on N-functional groups; pink-yellow and green-blue indicate the HOMO/LUMO (those symbols are defined as N-pyridinic (N-*py*), N-pyrolytic (N-*pyr*), N-graphitic (N-*q*), N-oxidized (N-*x*), N-amine primary, -secondary, and -tertiary (N-*p*, N-*s*, and N-*t*), and N-nitroso (N-*ni*) and -onitroso (N-*on*)).

positive correlations, respectively. Also, the significant levels can be calculated as shown in eq 6:

$$t = \frac{\rho_{vt}\sqrt{N-2}}{\sqrt{1-\rho_{vt}^{\ 2}}} \tag{6}$$

The *p*-value is achieved based on degrees of freedom (*N*-2), and "t" distribution. PCC can disclose the influence of inputs on the target (output), and thus, nonsignificant linear correlations can be deleted from the ML model process. Moreover, high collinearity of two variables may be observed, and the sensitivity observation can ascertain the specified impact on the target. Thenceforth, the DFT-based variables were utilized to train and test ML models to predict CH_4 adsorption energy performance.

2.7. The Accuracy Criteria. Two performance criteria, including R^2 and Root MSE (RMSE), were used to evaluate ML prediction accuracies for CH_4 adsorption energy (E_{ad}) predictions, which are defined as follows:

$$R^2 = 1 - \left(\sum_{1}^{N}(E_r - E_p)^2 / \sum_{1}^{N}(E_r - \hat{E}_r)^2\right) \tag{7}$$

$$\mathrm{RMSE} = \sqrt{\left(\sum_{r=1}^{N}|E_r - \hat{E}_p|^2\right)/(N-1)} \tag{8}$$

where E_r and E_p are the actual and predicted values, and $\hat{E}_r$ shows the average of the real values. R^2 and RMSE values close to 1 and 0, respectively, indicate that the model provides accurate predictions with reliable estimation errors.[79]

RESULTS AND DISCUSSION

3.1. DFT Calculation. *3.1.1. Nitrogen and Oxygen Functional Groups (N/O-x) Adsorbents.* Geometry optimization was applied to N/O functional groups and graphene structures as the primary task for the DFT calculation. PBE function estimated rms and max force in legible ranges with values 0 to 0.1, proving the high accuracy of the initial step of DFT calculations. As illustrated in Figure 5, three parameters are included in the optimization procedure: total energy, rms force, and max force. The total energy suggests differences in the stability and electronic properties of the nitrogen functional groups. Typically, the total energy is influenced by the electronic structure and the interaction between the functional groups and

https://doi.org/10.1021/acs.iecr.4c02626
Ind. Eng. Chem. Res. 2024, 63, 18940−18956

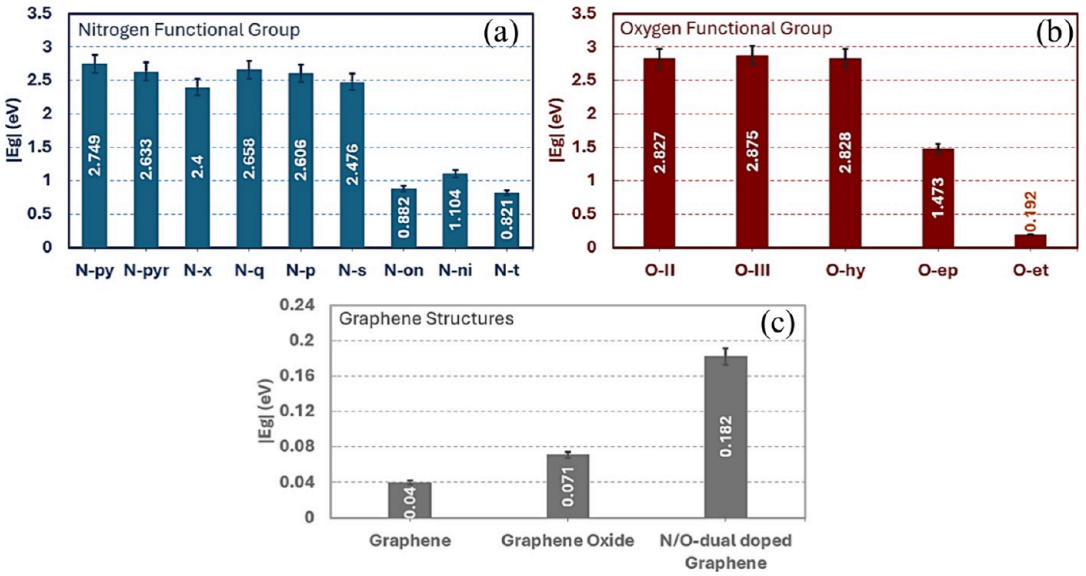

Figure 6. Comparative results of HOMO/LUMO energy gaps for CH_4 adsorption on (a) nitrogen functionality groups, (b) oxygen functionalities, and (c) graphene, graphene oxide (GO), and N-doped GO.

the graphene sheet.[80] All nitrogen functional group sites, excluding graphitic (N-*q*), demonstrated total energies of ∼24 eV (pyridinic, pyrolytic, graphitic, oxidized) and ∼27 eV (amine primary, -secondary, and -tertiary, nitroso, and onitroso). The geometry optimization procedure using DFT effectively established atoms of the molecular structures to take the most stable carbon matrix with the lowest possible ground state energy. Moreover, calculating the HOMO−LUMO energies provides insights into the electronic properties and reactivity of the nitrogen functionalities.[71] The energy trend from N-*py* increased from −2.65 to −2.05 eV in N-*pyr*, and it approximately continued for N-*x* and N-*q* in a stable trend of −2.73 and −2.58 eV. Comparatively, two nitrogen groups, N-*ni* and N-*on*, showed the lowest values, resulting from small HOMO−LUMO energy gaps. Also, the oxygen functionalities demonstrated the same values of total energies between 24 and 27 eV. The optimized structures of oxygen functional groups and the HOMO/LUMO energies of CH_4 uptake on O-functionalities are provided in Supporting Information (SI) Figure S1. The oxygen functional groups demonstrated −2.21/−5.0 eV, −2.37/−5.24 eV, −2.33/−5.16 eV, −3.59/−5.06 eV, and −3.2/−3.38 eV for LUMO−HOMO energies. To address the CH_4 adsorption, Osouleddini, and Rastegar presented the importance of energy gap (E_g) in infinite graphene adsorbent for CH_4 uptake. Although, the graphene sheets were expected as zero-gap semiconductors, the results showed the behavior with high similarity to semiconductor-like material with an E_g of about 0.32 eV.[81]

3.1.2. Graphene-Based Adsorbents (GO and N-GO). After the initial steps in energy and geometrical optimizations (DFT), calculations are applied to evaluate the interaction of CH_4 molecules with graphene-based adsorbents. The molecular schematics of optimized structures and HOMO/LUMO energies of CH_4 adsorption on graphene, GO, and N-doped GO are shown in Figure S2. Graphene structures are modified by doping oxygen and nitrogen on expanded sites on the graphene surface. Therefore, N/O functionalities merged in a simple graphene structure that generated graphene oxide (GO) and N/O dual-doped graphene (N-GO) (as shown in Figure 5). The HOMO−LUMO energy gaps for graphene, GO, and N-GO are achieved in negligible values of 0.04, 0.071, and 0.182 eV, respectively. The energy gaps (E_g) of the following adsorbents, including nitrogen-, oxygen functionalities, and graphene, are illustrated in Figure 6. E_g of the nine nitrogen functional groups, including N-*py*, N-*pyr*, N-*x*, N-*q*, N-*p*, and N-*s*, mainly exhibited the same E_g within 2.5 eV. On the other hand, three nitrogen functional groups of N-*on*, N-*ni*, and N-*t* obtained E_g values 0.88, 1.1, and 0.82 eV. Although, four oxygen functionalities such as O-*II*, O-*III*, O-*hy*, and O-*ep*, demonstrated E_g values of HOMO−LUMO ∼ 2.83, 2.88, 2.83, and 1.47 eV, O-*et* showed 0.192 eV. The negligible differences in HOMO−LUMO energy gaps of N-*on*, N-*ni*, N-*t*, and O-*et* functional groups can demonstrate high stability. It can describe the dynamism of π electrons in the aromatic systems that facilitate the electron transfer that can affect CH_4 uptake.[82]

Besides, three graphene structures disclosed small HOMO−LUMO energy gaps (E_g). These values are 0.04, 0.07, and 0.18 eV for graphene, GO, and N/O dual-doped graphene (N-GO), respectively. The calculations of geometrical and energy-based specifications (total energy, rms-/Max forces, HOMO−LUMO energies, etc.) were achieved for the above-mentioned adsorbent sites. Then, after primary analysis of DFT calculations, the CH_4 molecule was applied to each adsorbent to evaluate and achieve two significant adsorption specifications, such as optimal adsorption energy (E_{ad}) and distance (D_{ad}) for CH_4 physisorption.

3.1.3. CH_4 Adsorption on Heteroatoms Functionalities and Graphene-Based Adsorbents. The adsorption energy (E_{ad}) of nitrogen/oxygen functionalities and graphene structures (simple, oxide, N/O-co doped) are illustrated in Figure 7. The adsorption energies (E_{ad}) of N-functionalities at a distance of ∼2.0 Å achieved −2.28 and −2.44 eV for N-py and N-pyr, respectively. Also, some nitrogen functional groups between 2.7 and 3.1 Å obtained E_{ad} of −2.0, approximately −2.3, and −3 eV for (N-*on*, N-*p*, N-*ni*), (N-*py*, N-*Q*, N-*s*); and (N-*x* and N-*t*).

Oxygen functionalities absorbed the CH_4 molecule at a distance of 2.8 Å, and the adsorption energies achieved −3.03, −3.1, −3.26, and −3.43 eV adsorption energies. The adsorption of CH_4 is effectively applied in graphene, GO, and N-GO; the adsorption energies are equal to −2.43, −3.3, and −4.02 eV, respectively, to evaluate in-depth enough the DFT calculation.

https://doi.org/10.1021/acs.iecr.4c02626
Ind. Eng. Chem. Res. 2024, 63, 18940−18956

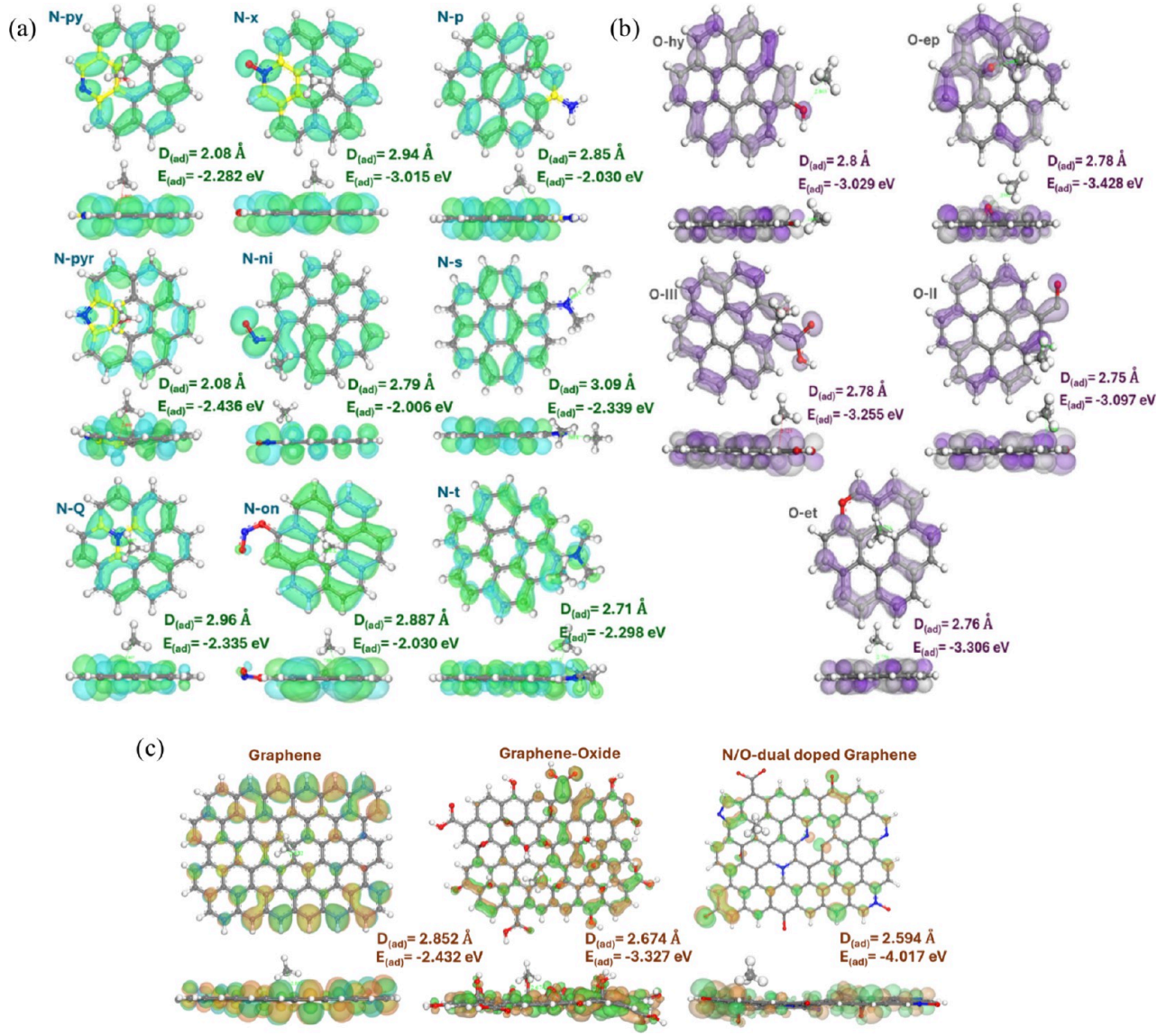

Figure 7. CH_4 adsorption on (a) pyridinic (N-*py*), pyrolytic (N-*pr*), graphitic (N-*q*), oxidized (N-*x*), amine primary, -secondary, and -tertiary (N-*p*, N-*s*, and N-*t*), nitroso (N-*ni*), and onitroso (N-*on*); (b) hydroxyl (O-*h*), carbonyl (O-*II*), carboxyl (O-*III*), epoxy (O-*x*), and ether (O-*eth*); and (c) graphene, graphene-oxide, and N/O-dual doped graphene.

3.2. Machine Learning Models for CH4 Adsorption Prediction. *3.2.1. Primary Statistical Analysis.* Analysis of Variance (ANOVA) is the most well-known primary statistical analysis used to evaluate the differences in adsorbent efficiency in CH_4 adsorption. Two critical diagnostic tools, the standard probability plot and the standardized residuals versus fits plot (see Figure S3). The histogram of standardized residuals versus frequency can confirm the usual assumption of the residuals for E_{ad} of CH_4 on adsorbents.

The independence of residuals can be examined by systematic patterns in a standardized residual-order plot (as can be seen in Figure S3). Then, to classify the adsorbent types, four comparative statistical methods, such as Tukey, Sidak, Fisher, and Bonferroni, were applied to sorting all adsorbents in groups based on their proficiency in CH_4 adsorption as shown in Figure 8. Although the mean values were mostly the same, the classifications of these methods mainly exhibited various classes of importance for CH_4 adsorption. The Pearson correlation coefficient (PCC) analysis is used to measure the strength and direction of the linear relationship between all variables, as shown in Figure 8. It is represented by PCC, denoted as *r*, which ranges from −1 to +1. PCC showed a strong linear relation between CH_4 adsorption and DE, RAE, TE, FT, and OS with 0.9, 0.89, −0.47, and 0.3 eV, respectively. These statistical methods facilitate the ML process that follows primary analysis, and five ML techniques can be applied to rediscover the methane adsorption energy. The following section discusses the ML modeling process with data sizes of 70%/30% for train/test phases, respectively, in CH_4 uptake on carbon-based solid adsorbents. The predictive accuracies of SVR, DT, MLP, and KNN are discussed. Moreover, sensitivity levels of adsorption features are evaluated based on the electronvolt (eV).

3.2.2. CH_4 Energy Adsorption Predictions by ML Models. After the primary statistical analysis, five ML models, including SVR, MLP, RF, DT, and KNN, were employed to estimate CH_4 energy adsorption. Four of these ML schemes that exhibited optimal predictive performances are illustrated in Figure 9. The predicted values of CH_4 energy adsorption were compared with

https://doi.org/10.1021/acs.iecr.4c02626
Ind. Eng. Chem. Res. 2024, 63, 18940−18956

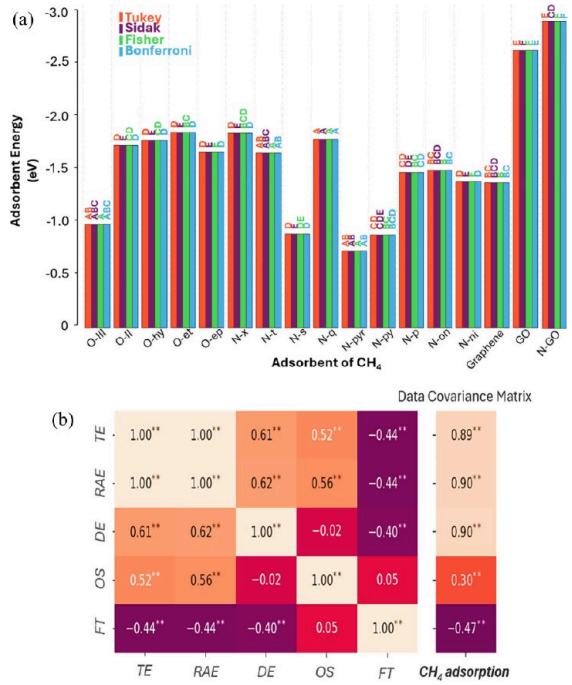

Figure 8. Illustration presents (a) the mean comparison results of CH_4 energy adsorption by four statistical methods on all N/O functionalities and graphene-based adsorbents (by using four statistical methods of Tukey, Sidak, Fisher, and Bonferroni); and (b) Pearson correlation on variables in CH_4 adsorption process.

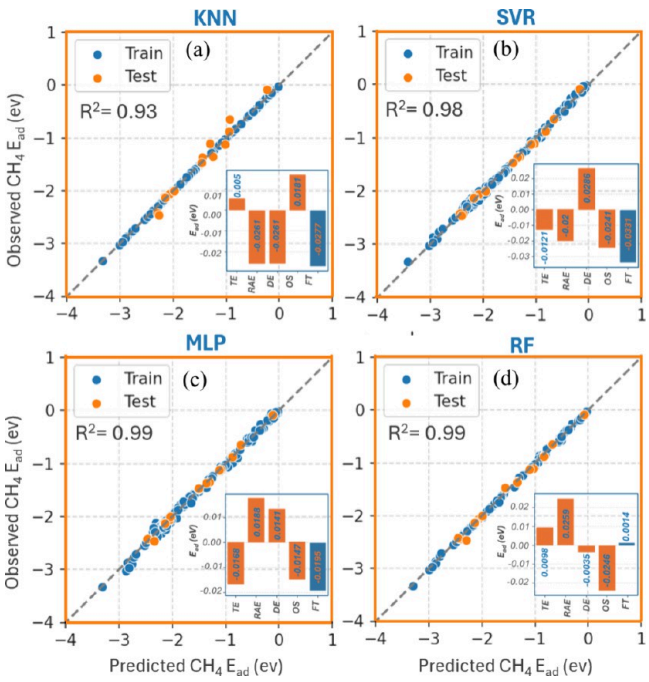

Figure 9. Predictive performance of ML models in CH_4 adsorption on adsorbent types (graphene, GO, N-GO), nitrogen/oxygen functional groups; (b) sensitivity analysis of adsorption characteristics; and (c) the correlation CH_4 adsorption features.

the best-fit line (well-known as a 45-degree line). This distribution implies the satisfactory predictive performance of ML models. According to the as-prepared data points in the training/test stages, well-appropriate agreements have been achieved between the actual and predicted results of E_{ad} in CH_4 adsorption in two train and test steps. MLP and RF models achieved high accuracy with an R^2 of 0.99 compared to SVR and KNN, which obtained 0.98 and 0.93, respectively. After ML models' predictions, as presented in Table 7, the sensitivity analysis (SA) displays the crucial levels of features such as total energy, rigid adsorption energy, deformation energy, optimized structure, and functionalities type (TE, RAE, DE, OS, and FT respectively) based on the five ML models. The SA approach applied in ML models indicates that SA-KNN showed high sensitivity on FT > RAE > and DE with −0.027 to −0.026 eV. Also, SA-SVR demonstrates the −0.033 eV significant level by excluding the functionality types (FT) that address the N/O functionality types for CH_4 adsorption. SA-MLP/-RF showed the importance level of features scaled between −0.025 to 0.025 eV.

3.3. Evaluation of ML Model Feasibility. Performance assessment is critical to the validation of ML models. In this study, ML models achieved a high fit on DFT-based predictions for the adsorption energy of CH_4 on various adsorbents. The predictive feasibility of ML models can be evaluated by the training size of the data set (TS) in train and test phases. As illustrated in Table 8, different ratios applied in TS in the 50 to 80% range can ensure reliable evaluations of the ML model's performance. The aim of the evaluation of feasibility in ML models was performed through two preprocessing data standardizations (Min/Max and *Z*-score normalization) by tuning TS at train and test steps.

Also, ML models exhibited an approximately close trend of RMSE increase by descending the data set size from 80% to 50% in the training phase. Although the RMSE comparatively increased by lowering the volume of training size in these ML models, they indicated that they have notable feasibility in CH_4 adsorption energy prediction. Also, the feasibility of the ML model in Z-score normalization was applied, in which SVR showed higher predictions than other ML models that changed from −0.07 to approximately −0.15 eV. The results presented in this study agree with the literature. In a previous study, RBF-DFT predicted E_{ad} of HOMO−LUMO in a range of −15.9 to −17.4 kJ mol^{-1}.[21] Nitrogen functionalities such as N-*X* and N-Q exhibited appropriate feasibility with ML with accuracies of ∼3.5% and 0.97−0.99 for MAPE and R^2, respectively.[21] SVR, RF, MLP, DT, and KNN combined with DFT to evaluate the rediscovery possibilities in methene E_{ad} on N/O functional groups with RMSEs of −0.14 to −0.05 and R^2 of 0.93 to 0.99. MLP model's results are plotted in 3D to evaluate the E_{ad} peaks based on the N/O functional groups and graphene structures, as shown in Figure 10. Nitrogen and oxygen functional groups of N-*py*, N-*x*, and O-*hy* performed −2 to −3 eV by nine runs for optimizing structure. The visualization of predicted values demonstrates the peaks of adsorption energy in DFT calculation with an accuracy of 0.99 for R^2 and ∼0.06 of RMSE. Figure 10 shows the total and deformation energies (E_{total} and E_{def}) based on the N/O heteroatoms functionalities, graphene, graphene oxide (GO), and N-doped GO. The GO and N-GO approximately showed approximately −3 to −3.2 eV for E_{total} by MLP model. On the other hand, the other N/O groups demonstrated accurate predictive results compared to E_{ad}. Also, N-*x* achieved the lowest E_{def} within approximately −3 eV compared with other adsorbents (as seen in Figure 11). Therefore, the 3D plots indicate the overall stability of the CH_4 adsorption process; the lower values of total E_{ads} suggest more stable configurations. Moreover, the higher values of E_{def} highlight the structural changes that occur upon adsorption.

https://doi.org/10.1021/acs.iecr.4c02626
Ind. Eng. Chem. Res. 2024, 63, 18940−18956

Table 7. ML Model'S Prediction Accuracies and Sensitivity Analysis

Prediction		Sensitivity Levels				
ML model	Accuracy (R^2)	TE	RAE	DE	OS	FT
SVR	0.989	−0.0121	−0.02	0.0286	−0.0241	−0.0331
DT	0.968	−0.021	0.001	−0.015	0.0179	−0.009
MLP	0.998	−0.0168	0.0188	0.0141	−0.0147	−0.0195
RF	0.986	0.0098	0.0259	−0.0035	−0.0246	0.0014
KNN	0.931	0.005	−0.0261	−0.0261	0.0181	−0.0277

Table 8. ML Models Feasibility Evaluation by Tuning Training Size (TS) Based on the RMSE Criteria

		80%/20%		70%/30%		60%/40%		50%/50%	
Preprocess Method of Data (RMSE)	ML model (E_{ad})	Train	Test	Train	Test	Train	Test	Train	Test
Min/Max	SVR	−0.0627	−0.0570	−0.0846	−0.0847	−0.1579	−0.1285	−0.1974	−0.2016
	RF	−0.0788	−0.0606	−0.0963	−0.0840	−0.1367	−0.1177	−0.2037	−0.2159
	MLP	−0.0529	−0.0502	−0.1025	−0.0921	−0.1477	−0.1292	−0.1986	−0.1778
	DT	−0.0954	−0.0729	−0.1324	−0.1740	−0.1536	−0.2096	−0.2109	−0.2233
	KNN	−0.1362	−0.1549	−0.1505	−0.1746	−0.1617	−0.1495	−0.1911	−0.2673
Z-score normalization	SVR	−0.0713	−0.0945	−0.0962	−0.1091	−0.1131	−0.1354	−0.1442	−0.1512
	RF	−0.0513	−0.0609	−0.0642	−0.0785	−0.0913	−0.1120	−0.1598	−0.1839
	MLP	−0.133	−0.1148	−0.1219	−0.1214	−0.1406	−0.1044	−0.2019	−0.2108
	DT	−0.091	−0.0787	−0.1120	−0.1089	−0.1851	−0.1721	−0.2266	−0.2683
	KNN	−0.1018	−0.1329	−0.1370	−0.1564	−0.1472	−0.1597	−0.3421	−0.3290

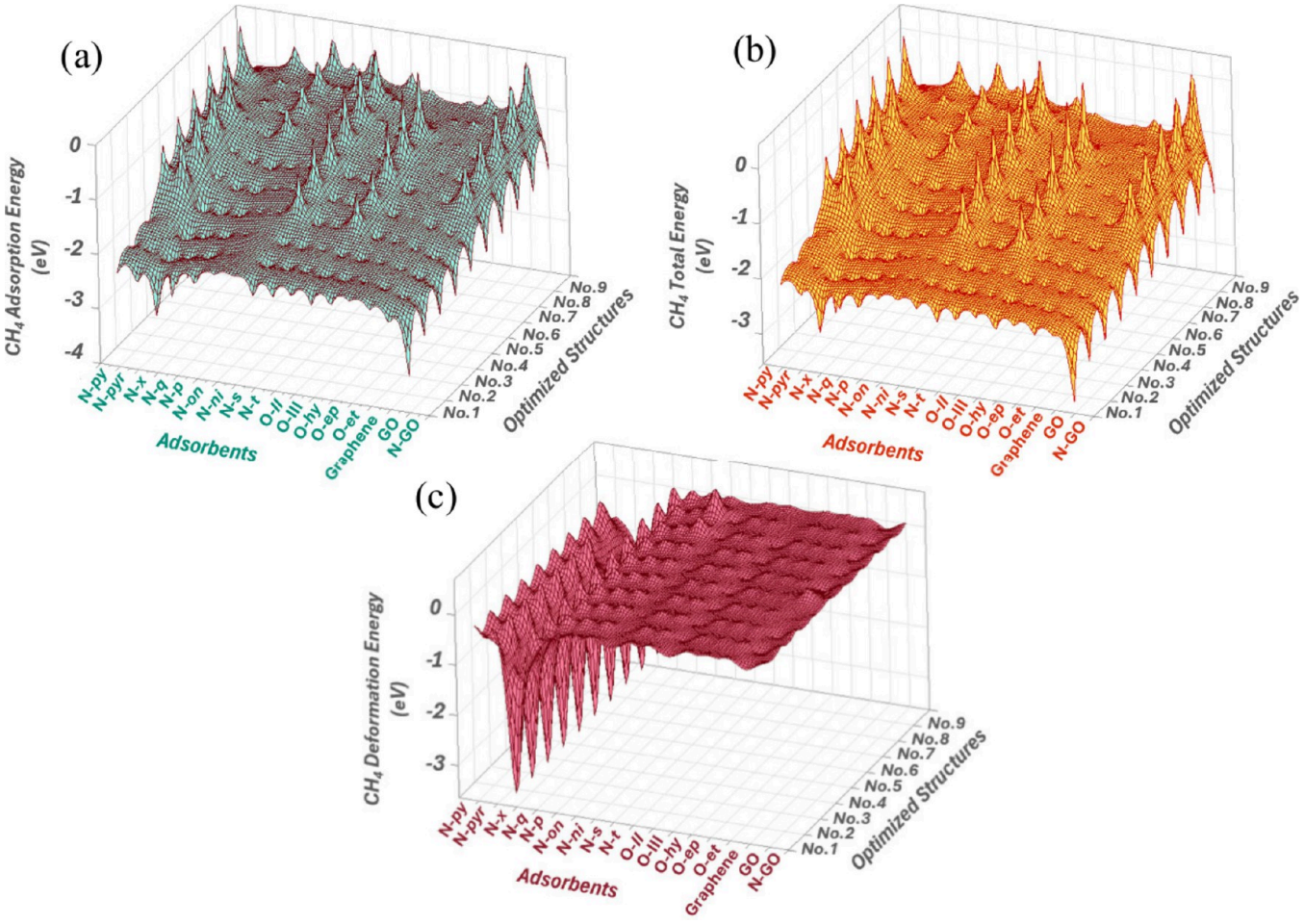

Figure 10. 3D plots of MLP-predicted CH_4 adsorptive properties for (a) adsorption energy, (b) total energy, and (c) deformation energy (based on the optimized structures, N/O and graphene adsorbents, and three adsorption energies of the CH_4 molecule).

Finally, all energy criteria in the CH_4 uptake process are effectively affected by the type and number of optimized nitrogen- and oxygen-containing groups and graphene as adsorbents.

https://doi.org/10.1021/acs.iecr.4c02626
Ind. Eng. Chem. Res. 2024, 63, 18940−18956

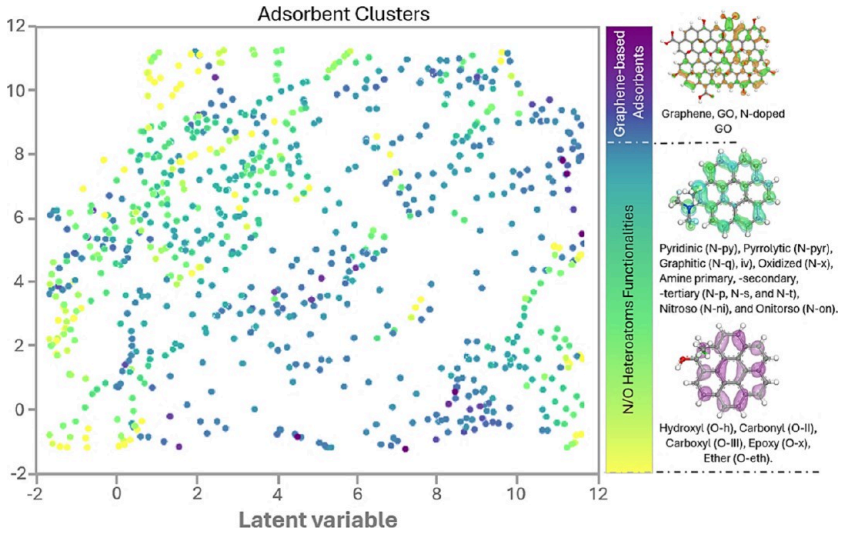

Figure 11. UMAP histography illustrating the clusters and structure of data sets of E_{ad} of CH_4 adsorption on N/O functional groups and graphene structures.

3.4. Adsorbent Screening and Future Outlook. After DFT and supervised ML models, the Uniform Manifold Approximation and Projection (UMAP) technique can provide new insights into the gas adsorption field. The UMAP method was employed to visualize CH_4 uptake by screening and clustering the adsorbent types of N/O functionalities and graphene-based structures. UMAP discloses the numerical gaps and space in the data sets. As shown in Figure 11, UMAP illustrates the structure of data sets and adsorbent clusters based on the heteroatom functionalities and graphene structures. Although the adsorbents are limited to graphene and N/O functional groups, UMAP facilitated the disentanglement of the adsorbent structures, enabling a clearer visualization of the relationships between the heteroatom functional groups and graphene-based structures in terms of CH_4 uptake. Hence, by combining UMAP with ML models, large data sets can be explored for advanced adsorbent material, which can lead to the discovery of new materials with optimal properties for CH_4 adsorption. Also, UMAP can reduce the dimensionality of complex data sets to identify patterns and relationships by enhancing the predictive accuracies of ML models for material design.[83] Moreover, adsorbents tailored to specific conditions and requirements can be designed using predictive models enhanced by UMAP. This can lead to creating materials optimized for particular applications, such as natural gas storage or environmental remediation.[84]

CONCLUSION

This study's methane physisorption performance was synergistically modeled and rediscovered by DFT and multi-ML techniques, respectively. Multiple graphene structures and nitrogen/oxygen functional groups such as pyridinic, pyrolytic, nitroso, epoxy (O-*x*), ether (O-*eth*), etc. were employed for CH_4 uptake. N/O functional groups demonstrated −2.21/−5.0 eV for the LUMO−HOMO energies. Also, energy gaps for graphene, graphene oxide, and N-GO are achieved at negligible values of 0.04, 0.071, and 0.182 eV, respectively. The adsorption energies (E_{ad}) of N/O-functionalities in the distance of ∼2.0 to 3.1 Å groups obtained E_{ad} of approximately −2.0 to −4. eV adsorption energies. Five ML schemes comparatively performed highly accurate prediction and rediscovery of CH_4 physisorption by utilizing the multiadsorptive features of optimized adsorbents with an R^2 of 0.99. Also, the sensitivity analysis was applied to five adsorption features based on the optimized structure of N/O functionalities and graphene structures. The sensitivity levels of input features were determined from −0.03 to 0.02 eV. UMAP rediscovered and screened the functionalities of graphene as CH_4 adsorbents. As a further outlook, multi-ML/DFT/and UMAP techniques can be employed as a predictive route to estimate gas physisorption storage for advanced solid adsorbents such as MXene and polymer/carbon-based composites.

ASSOCIATED CONTENT

Supporting Information

The Supporting Information is available free of charge at https://pubs.acs.org/doi/10.1021/acs.iecr.4c02626.

The statistical results of ANOVA analysis, geometry optimization processes, and HOMO−LUMO energies for CH_4 adsorption (PDF)

AUTHOR INFORMATION

Corresponding Author

Shakirudeen A. Salaudeen − *Department of Mechanical Engineering, McMaster University, Hamilton, Ontario L8S 3L8, Canada;* orcid.org/0000-0001-6046-4366; Email: salaudes@mcmaster.ca

Authors

Mohammad Rahimi − *Department of Mechanical Engineering, McMaster University, Hamilton, Ontario L8S 3L8, Canada*

Amir Mehrpanah − *Department of Computer Science, Royal Institute of Technology, 114 28 Stockholm, Sweden*

Parastoo Mouchani − *Department of Chemical Engineering & Applied Chemistry, University of Toronto, Toronto, Ontario M5S 1A1, Canada*

Ehsan Rahimi − *Department of Materials Science and Engineering, Delft University of Technology, 2628 CD Delft, The Netherlands;* orcid.org/0000-0002-7128-8940

Complete contact information is available at: https://pubs.acs.org/10.1021/acs.iecr.4c02626

Notes

The authors declare no competing financial interest.

■ ACKNOWLEDGMENTS

The authors acknowledge the financial support from the Discovery Grant by the Natural Sciences and Engineering Research Council of Canada (NSERC, Grant number: RGPIN-2023-04754).

■ REFERENCES

(1) Lozano-Castello, D.; Alcaniz-Monge, J.; De La Casa-Lillo, M.; Cazorla-Amorós, D.; Linares-Solano, A. Advances in the study of methane storage in porous carbonaceous materials. *Fuel* **2002**, *81* (14), 1777−1803.

(2) Roy, N.; Yasmin, S.; Mohiuddin, A. K.; Jeon, S. Pyridinic and Pyrrolic-N induced carbon nanotubes support bimetallic oxide nanoparticles as high-performance electrocatalysts for oxygen reduction reaction. *Applied Surface Science Advances* **2023**, *18*, No. 100517.

(3) Choi, S.; Alkhabbaz, M. A.; Wang, Y.; Othman, R. M.; Choi, M. Unique thermal contraction of zeolite-templated carbons enabling micropore size tailoring and its effects on methane storage. *Carbon* **2019**, *141*, 143−153.

(4) Wang, Z.; Duan, J.; Chen, S.; Fu, Y.; Li, X.; Wang, D.; Zhang, M.; Zhang, Z.; Liu, D.; Wang, F. A review on high-density methane storage in confined nanospace by adsorption-hydration hybrid technology. *Journal of Energy Storage* **2022**, *50*, No. 104195.

(5) Memetova, A.; Tyagi, I.; Karri, R. R.; Kumar, V.; Tyagi, K.; Suhas; Memetov, N.; Zelenin, A.; Pasko, T.; Gerasimova, A.; et al. Porous carbon-based material as a sustainable alternative for the storage of natural gas (methane) and biogas (biomethane): A review. *Chemical Engineering Journal* **2022**, *446*, No. 137373.

(6) Zhu, X.; Yellezuome, D.; Wang, Z.; Liu, R. Functionalized polyethyleneimine grafted magnetic biochar for facilitating in-situ CO2 conversion to improve methane production in thermophilic anaerobic digestion. *Fuel* **2024**, *360*, No. 130493.

(7) Choi, P.-S.; Jeong, J.-M.; Choi, Y.-K.; Kim, M.-S.; Shin, G.-J.; Park, S.-J. A review: methane capture by nanoporous carbon materials for automobiles. *Carbon letters* **2016**, *17* (1), 18−28.

(8) Wu, Z.; Wee, V.; Ma, X.; Zhao, D. Adsorbed natural gas storage for onboard applications. *Advanced Sustainable Systems* **2021**, *5* (4), No. 2000200.

(9) Jackson, R. B.; Saunois, M.; Bousquet, P.; Canadell, J. G.; Poulter, B.; Stavert, A. R.; Bergamaschi, P.; Niwa, Y.; Segers, A.; Tsuruta, A. Increasing anthropogenic methane emissions arise equally from agricultural and fossil fuel sources. *Environmental Research Letters* **2020**, *15* (7), No. 071002.

(10) Safarzadeh Khosrowshahi, M.; Afshari Aghajari, A.; Rahimi, M.; Maleki, F.; Ghiyabi, E.; Rezanezhad, A.; Bakhshi, A.; Salari, E.; Shayesteh, H.; Mohammadi, H. Recent Progress on Advanced Solid Adsorbents for CO2 Capture: From Mechanism to Machine Learning. *Materials Today Sustainability* **2024**, *27*, No. 100900.

(11) Chandra, N.; Patra, P. K.; Fujita, R.; Höglund-Isaksson, L.; Umezawa, T.; Goto, D.; Morimoto, S.; Vaughn, B. H.; Röckmann, T. Methane emissions decreased in fossil fuel exploitation and sustainably increased in microbial source sectors during 1990−2020. *Communications Earth & Environment* **2024**, *5* (1), 147.

(12) Thanh, H. V.; Ebrahimnia Taremsari, S.; Ranjbar, B.; Mashhadimoslem, H.; Rahimi, E.; Rahimi, M.; Elkamel, A. Hydrogen storage on porous carbon adsorbents: rediscovery by nature-derived algorithms in random forest machine learning model. *Energies* **2023**, *16* (5), 2348.

(13) Pribylov, A.; Fomkin, A.; Shkolin, A.; Men'shchikov, I. Adsorption of Methane onto Microporous Activated Carbon in a Volumetric Storage System. *Protection of Metals and Physical Chemistry of Surfaces* **2023**, *59* (1), 14−18.

(14) Sun, J.; Ju, J.; Chen, Y.; Chen, L.; Chen, Z.; Chen, C. Co-adsorption of hydrogen and methane can improve the energy storage capacity of Mn-modified graphene. *Journal of Energy Storage* **2023**, *63*, No. 106973.

(15) Safaei-Farouji, M.; Vo Thanh, H.; Dai, Z.; Mehbodniya, A.; Rahimi, M.; Ashraf, U.; Radwan, A. E. Exploring the power of machine learning to predict carbon dioxide trapping efficiency in saline aquifers for carbon geological storage project. *Journal of Cleaner Production* **2022**, *372*, No. 133778.

(16) Blankenship, L. S.; Mokaya, R. Modulating the porosity of carbons for improved adsorption of hydrogen, carbon dioxide, and methane: a review. *Materials Advances* **2022**, *3* (4), 1905−1930.

(17) Rahimi, M.; Abbaspour-Fard, M. H.; Rohani, A. Machine learning approaches to rediscovery and optimization of hydrogen storage on porous bio-derived carbon. *Journal of Cleaner Production* **2021**, *329*, No. 129714.

(18) Zöttl, S.; Kaiser, A.; Bartl, P.; Leidlmair, C.; Mauracher, A.; Probst, M.; Denifl, S.; Echt, O.; Scheier, P. Methane adsorption on graphitic nanostructures: every molecule counts. *journal of physical chemistry letters* **2012**, *3* (18), 2598−2603.

(19) González, S.; Vines, F.; García, J. F.; Erazo, Y.; Illas, F. A DF-vdW study of the CH4 adsorption on different Ni surfaces. *Surface science* **2014**, *625*, 64−68.

(20) Khosrowshahi, M. S.; Mashhadimoslem, H.; Shayesteh, H.; Singh, G.; Khakpour, E.; Guan, X.; Rahimi, M.; Maleki, F.; Kumar, P.; Vinu, A. Natural products derived porous carbons for CO2 capture. *Advanced Science* **2023**, *10* (36), No. 2304289.

(21) Rahimi, M.; Abbaspour-Fard, M. H.; Rohani, A.; Yuksel Orhan, O.; Li, X. Modeling and optimizing N/O-enriched bio-derived adsorbents for CO2 capture: machine learning and DFT calculation approaches. *Ind. Eng. Chem. Res.* **2022**, *61* (30), 10670−10688.

(22) Li, K.; Li, H.; Li, N.; Song, Q.; Qi, L. Dissociation mechanisms of CH4 on pristine, N-doped and vacancy graphene by DFT study. *Diamond Relat. Mater.* **2021**, *114*, No. 108323.

(23) Homayoonnia, S.; Phani, A.; Kim, S. MOF/MWCNT−nanocomposite manipulates high selectivity to gas via different adsorption sites with varying electron affinity: a study in methane detection in parts-per-billion. *ACS sensors* **2022**, *7* (12), 3846−3856.

(24) Park, S.; Yang, J.; Lee, H.-M.; Lee, Y.-S.; Lee, Y. K.; Yamada, Y.; Lee, N.; Kim, J. Effect of the Position of Amine Groups on the CO2, CH4, and H2 Adsorption Performance of Graphene Nanoflakes. *Ind. Eng. Chem. Res.* **2023**, *62* (12), 5230−5240.

(25) Zhao, X.; Feng, S.; Li, S.; Hu, Y.; Wang, W.; Zhang, X.; Zhang, Q.; Chen, Y.; Liu, J.; Ma, L. The role of primary amines in modified chitosan to enhance the aldol condensation of biomass-derived carbonyl compounds. *Fuel* **2023**, *351*, No. 128820.

(26) Liao, J.; Yazaydin, A. O.; Yang, S.; Li, F.; Ding, L. Molecular simulation studies of hydrogen enriched methane (HEM) storage in Covalent Organic Frameworks. *Microporous Mesoporous Mater.* **2016**, *231*, 138−146.

(27) Yang, W.; Wang, Y.; Yan, F.; Si, G.; Lin, B. Evolution characteristics of coal microstructure and its influence on methane adsorption capacity under high temperature pyrolysis. *Energy* **2022**, *254*, No. 124262.

(28) Mahmoudian, L.; Rashidi, A.; Dehghani, H.; Rahighi, R. Single-step scalable synthesis of three-dimensional highly porous graphene with favorable methane adsorption. *Chemical Engineering Journal* **2016**, *304*, 784−792.

(29) Albesa, A. G.; Llanos, J. L.; Vicente, J. L. Comparative Study of Methane Adsorption on Graphite. *Langmuir* **2008**, *24* (8), 3836−3840.

(30) Dutta, D.; Wood, B. C.; Bhide, S. Y.; Ayappa, K. G.; Narasimhan, S. Enhanced Gas Adsorption on Graphitic Substrates via Defects and Local Curvature: A Density Functional Theory Study. *J. Phys. Chem. C* **2014**, *118* (15), 7741−7750.

(31) Wang, W.; Han, Z.; Wang, H.; Wei, X.; Zhong, R.; Qi, J. Construction of Co/Mn-based nanowires with adjustable surface state for boosting lean methane catalytic oxidation. *Ceram. Int.* **2024**, *50* (1), 2293−2302.

(32) Hassani, A.; Mosavian, M. T. H.; Ahmadpour, A.; Farhadian, N. A comparative theoretical study of methane adsorption on the nitrogen, boron and lithium doped graphene sheets including density functional

https://doi.org/10.1021/acs.iecr.4c02626
Ind. Eng. Chem. Res. 2024, 63, 18940−18956

dispersion correction. *Computational and Theoretical Chemistry* **2016**, *1084*, 43−50.
(33) Jia, J.; Wu, Y.; Zhao, D.; Li, B.; Wang, D.; Wang, F. Adsorption of CH4/CO2/N2 by different functional groups in coal. *Fuel* **2023**, *335*, No. 127062.
(34) Song, X.; Wang, L. a.; Gong, J.; Zhan, X.; Zeng, Y. Exploring a new method to study the effects of surface functional groups on adsorption of CO2 and CH4 on activated carbons. *Langmuir* **2020**, *36* (14), 3862−3870.
(35) Wadi, B.; Li, C.; Manovic, V.; Moghadam, P.; Nabavi, S. A. Contributions of CH4-amine interactions by primary, secondary, and tertiary amines on CO2/CH4 separation efficiency. *Chemical Engineering Journal* **2023**, *463*, No. 142117.
(36) Lazar, P.; Mach, R.; Otyepka, M. Spectroscopic fingerprints of graphitic, pyrrolic, pyridinic, and chemisorbed nitrogen in N-doped graphene. *J. Phys. Chem. C* **2019**, *123* (16), 10695−10702.
(37) Chen, L.-Y.; Yu, B.-Y.; Xie, Y.; Wang, S.-F.; Zhang, J.-M. Tuning gas-sensitive properties of the twin graphene decorated with transition metal via small electrical field: A viewpoint of first principle. *Diamond Relat. Mater.* **2023**, *133*, No. 109707.
(38) Oguz Erdogan, F. A comparative study on methane adsorption onto various adsorbents including activated carbons, zeolites, MWCNT, and MCM-41. *International Journal of Coal Preparation and Utilization* **2022**, *42* (7), 2078−2098.
(39) Mollaamin, F.; Monajjemi, M. Doping of graphene nanostructure with iron, nickel and zinc as selective detector for the toxic gas removal: A density functional theory study. *C* **2023**, *9* (1), 20.
(40) Nematollahi, P.; Neyts, E. C. Direct methane conversion to methanol on M and MN4 embedded graphene (M= Ni and Si): A comparative DFT study. *Appl. Surf. Sci.* **2019**, *496*, No. 143618.
(41) Nematollahi, P.; Neyts, E. C. Direct oxidation of methane to methanol on Co embedded N-doped graphene: Comparing the role of N2O and O2 as oxidants. *Applied Catalysis A: General* **2020**, *602*, No. 117716.
(42) Zhang, H.; Thanh, H. V.; Rahimi, M.; Al-Mudhafar, W. J.; Tangparitkul, S.; Zhang, T.; Dai, Z.; Ashraf, U. Improving predictions of shale wettability using advanced machine learning techniques and nature-inspired methods: Implications for carbon capture utilization and storage. *Science of The Total Environment* **2023**, *877*, No. 162944.
(43) Zhang, C.; Li, D.; Xie, Y.; Stalla, D.; Hua, P.; Nguyen, D. T.; Xin, M.; Lin, J. Machine learning assisted rediscovery of methane storage and separation in porous carbon from material literature. *Fuel* **2021**, *290*, No. 120080.
(44) Meng, M.; Qiu, Z.; Zhong, R.; Liu, Z.; Liu, Y.; Chen, P. Adsorption characteristics of supercritical CO2/CH4 on different types of coal and a machine learning approach. *Chemical Engineering Journal* **2019**, *368*, 847−864.
(45) Han, Y.; Zhao, J.; Guo, X.; Jiao, T. Enhanced Methane Storage in Graphene Oxide Induced by an External Electric Field: A Study by MD Simulations and DFT Calculation. *Langmuir* **2023**, *39* (22), 7648−7659.
(46) Mahlaba, S. V.; Govender, A.; Leteba, G. M.; van Steen, E. The Highly Selective, Aerobic Oxidation of Methane to Formaldehyde over Pt Supported on Carbon: Activity, Selectivity and Stability. *ChemistrySelect* **2023**, *8* (48), No. e202304616.
(47) Huang, W.; Wang, H.; Zhou, J.; Wang, J.; Duchesne, P. N.; Muir, D.; Zhang, P.; Han, N.; Zhao, F.; Zeng, M.; et al. Highly active and durable methanol oxidation electrocatalyst based on the synergy of platinum−nickel hydroxide−graphene. *Nat. Commun.* **2015**, *6* (1), 10035.
(48) Anithaa, V.; Shankar, R.; Vijayakumar, S. DFT-based investigation on adsorption of methane on pristine and defected graphene. *Structural Chemistry* **2017**, *28*, 1935−1952.
(49) Kandagal, V. S.; Pathak, A.; Ayappa, K.; Punnathanam, S. N. Adsorption on edge-functionalized bilayer graphene nanoribbons: assessing the role of functional groups in methane uptake. *J. Phys. Chem. C* **2012**, *116* (44), 23394−23403.
(50) Seema, H.; Kemp, K. C.; Le, N. H.; Park, S.-W.; Chandra, V.; Lee, J. W.; Kim, K. S. Highly selective CO2 capture by S-doped microporous carbon materials. *Carbon* **2014**, *66*, 320−326.
(51) He, X.; Gui, Y.; Xie, J.; Liu, X.; Wang, Q.; Tang, C. A DFT study of dissolved gas (C2H2, H2, CH4) detection in oil on CuO-modified BNNT. *Appl. Surf. Sci.* **2020**, *500*, No. 144030.
(52) Altundal, O. F.; Haslak, Z. P.; Keskin, S. Combined GCMC, MD, and DFT approach for unlocking the performances of COFs for methane purification. *Ind. Eng. Chem. Res.* **2021**, *60* (35), 12999−13012.
(53) Ghanbari, R.; Safaiee, R.; Golshan, M. A dispersion-corrected DFT investigation of CH4 adsorption by silver-decorated monolayer graphene in the presence of ambient oxygen molecules. *Appl. Surf. Sci.* **2018**, *457*, 303−314.
(54) Wei, X.; Peng, D.; Shen, L.; Ai, Y.; Lu, Z. Analyzing of metal organic frameworks performance in CH4 adsorption using machine learning techniques: A GBRT model based on small training dataset. *Journal of Environmental Chemical Engineering* **2023**, *11* (3), No. 110086.
(55) Yuan, X.; Suvarna, M.; Low, S.; Dissanayake, P. D.; Lee, K. B.; Li, J.; Wang, X.; Ok, Y. S. Applied machine learning for prediction of CO2 adsorption on biomass waste-derived porous carbons. *Environ. Sci. Technol.* **2021**, *55* (17), 11925−11936.
(56) Vo Thanh, H.; Zhang, H.; Rahimi, M.; Ashraf, U.; Migdady, H.; Daoud, M. S.; Abualigah, L. Enhancing Carbon Sequestration: Innovative Models for Wettability Dynamics in CO2-Brine-Mineral Systems. *Journal of Environmental Chemical Engineering* **2024**, *12*, No. 113435.
(57) Ohtsubo, N.; Gohda, S.; Gotoh, K.; Sato, S.; Yamada, Y. Bottom-up synthesis of pyridinic nitrogen-containing carbon materials with C−H groups next to pyridinic nitrogen from two-ring aromatics. *Carbon* **2023**, *207*, 270−291.
(58) Lalitha, M.; Lakshmipathi, S. Gas adsorption efficacy of graphene sheets functionalised with carboxyl, hydroxyl and epoxy groups in conjunction with Stone−Thrower−Wales (STW) and inverse Stone−Thrower−Wales (ISTW) defects. *Phys. Chem. Chem. Phys.* **2017**, *19* (45), 30895−30913.
(59) Duan, C.; Liu, F.; Nandy, A.; Kulik, H. J. Putting density functional theory to the test in machine-learning-accelerated materials discovery. *J. Phys. Chem. Lett.* **2021**, *12* (19), 4628−4637.
(60) Baird, S. G.; Diep, T. Q.; Sparks, T. D. DiSCoVeR: a materials discovery screening tool for high performance, unique chemical compositions. *Digital Discovery* **2022**, *1* (3), 226−240.
(61) Damte, J. Y.; Hailu, Y. M.; Cammarata, A. Formation of ethane by activation of methane on B, N co-doped graphene surface decorated by Ir13 cluster: A first principle study. *Appl. Surf. Sci.* **2024**, *654*, No. 159524.
(62) Wang, Z.; Liu, J.; Yang, Y.; Yu, Y.; Yan, X.; Zhang, Z. Insights into the catalytic behavior of LaMnO3 perovskite for Hg0 oxidation by HCl. *Journal of hazardous materials* **2020**, *383*, No. 121156.
(63) Blöchl, P. E. Projector augmented-wave method. *Phys. Rev. B* **1994**, *50* (24), 17953.
(64) Xu, Y.; Hu, Z.; Liu, Z.; Zhu, H.; Yan, Y.; Xu, J.; Yang, C. Molecular simulations on tuning the interlayer spacing of graphene nanoslits for C4H6/C4H10 separation. *ACS Applied Nano Materials* **2021**, *4* (2), 1994−2001.
(65) Rahimi, M.; Pourramezan, M.-R.; Rohani, A. Modeling and classifying the in-operando effects of wear and metal contaminations of lubricating oil on diesel engine: A machine learning approach. *Expert Systems with Applications* **2022**, *203*, No. 117494.
(66) Akdaş, S. B.; Fişne, A. A data-driven approach for the prediction of coal seam gas content using machine learning techniques. *Applied Energy* **2023**, *347*, No. 121499.
(67) Whitehead, S. D.; Ballard, D. H. Learning to perceive and act by trial and error. *Machine Learning* **1991**, *7*, 45−83.
(68) Zhang, H.; Wang, P.; Rahimi, M.; Vo Thanh, H.; Wang, Y.; Dai, Z.; Zheng, Q.; Cao, Y. Catalyzing net-zero carbon strategies: Enhancing CO2 flux Prediction from underground coal fires using optimized

machine learning models. *Journal of Cleaner Production* **2024**, *441*, No. 141043.
(69) Torres, J. F.; Gutiérrez-Avilés, D.; Troncoso, A.; Martínez-Álvarez, F. Random hyper-parameter search-based deep neural network for power consumption forecasting. In *Proceedings of the Advances in Computational Intelligence: 15th International Work-Conference on Artificial Neural Networks, IWANN 2019*; Gran Canaria, Spain, June 12−14, 2019 ; Springer, 2019: Part I 15, pp 259−269.
(70) Rahimi, M.; Abbaspour-Fard, M. H.; Rohani, A. Synergetic effect of N/O functional groups and microstructures of activated carbon on supercapacitor performance by machine learning. *J. Power Sources* **2022**, *521*, No. 230968.
(71) Vo Thanh, H.; Rahimi, M.; Tangparitkul, S.; Promsuk, N. Modeling the thermal transport properties of hydrogen and its mixtures with greenhouse gas impurities: A data-driven machine learning approach. *Int. J. Hydrogen Energy* **2024**, *83*, 1−12.
(72) Vakil-Baghmisheh, M.-T.; Pavešić, N. A fast simplified fuzzy ARTMAP network. *Neural processing letters* **2003**, *17*, 273−316.
(73) Rahimi, M.; Abbaspour-Fard, M. H.; Rohani, A. A multi-data-driven procedure towards a comprehensive understanding of the activated carbon electrodes performance (using for supercapacitor) employing ANN technique. *Renewable Energy* **2021**, *180*, 980−992.
(74) Vakili, A. R.; Ehtesham, S.; Danesh-Mesgaran, M.; Rohani, A.; Rahimi, M. Toward modeling the in vitro gas production process by using propolis extract oil treatment: machine learning and kinetic models. *Ind. Eng. Chem. Res.* **2023**, *62* (37), 14910−14922.
(75) Kotsiantis, S. B.; Zaharakis, I.; Pintelas, P. Supervised machine learning: A review of classification techniques. *Frontiers Artificial Intelligence Applications* **2007**, *160* (1), 3−24.
(76) Suthaharan, S.; Suthaharan, S. Decision tree learning. *Machine Learning Models and Algorithms for Big Data Classification: Thinking with Examples for Effective Learning* **2016**, *36*, 237−269.
(77) Vo Thanh, H.; Rahimi, M.; Dai, Z.; Zhang, H.; Zhang, T. Predicting the wettability rocks/minerals-brine-hydrogen system for hydrogen storage: Re-evaluation approach by multi-machine learning scheme. *Fuel* **2023**, *345*, No. 128183.
(78) Zhu, X.; Huang, Z.; Shen, H. T.; Zhao, X. Linear cross-modal hashing for efficient multimedia search. *Proceedings of the 21st ACM international conference on Multimedia*; Association for Computing Machinery, 2013; pp 143−152.
(79) Rahimi, M.; Mashhadimoslem, H.; Vo Thanh, H.; Ranjbar, B.; Safarzadeh Khosrowshahi, M.; Rohani, A.; Elkamel, A. Yield prediction and optimization of biomass-based products by multi-machine learning schemes: Neural, regression and function-based techniques. *Energy* **2023**, *283*, No. 128546.
(80) Sreeprasad, T.; Berry, V. How do the electrical properties of graphene change with its functionalization? *small* **2013**, *9* (3), 341−350.
(81) Osouleddini, N.; Rastegar, S. F. DFT study of the CO2 and CH4 assisted adsorption on the surface of graphene. *J. Electron Spectrosc. Relat. Phenom.* **2019**, *232*, 105−110.
(82) Shimizu, A.; Ishizaki, Y.; Horiuchi, S.; Hirose, T.; Matsuda, K.; Sato, H.; Yoshida, J.-i. HOMO−LUMO energy-gap tuning of π-conjugated zwitterions composed of electron-donating anion and electron-accepting cation. *Journal of Organic Chemistry* **2021**, *86* (1), 770−781.
(83) Qu, J.; Xie, Y. R.; Ciesielski, K. M.; Porter, C. E.; Toberer, E. S.; Ertekin, E. Leveraging language representation for materials exploration and discovery. *npj Computational Materials* **2024**, *10* (1), 58.
(84) Wu, X.; Cao, Z.; Lu, X.; Cai, W. Prediction of methane adsorption isotherms in metal−organic frameworks by neural network synergistic with classical density functional theory. *Chemical Engineering Journal* **2023**, *459*, No. 141612.

https://doi.org/10.1021/acs.iecr.4c02626
Ind. Eng. Chem. Res. 2024, 63, 18940−18956